OPEN ACCESS
Journal of Theoretical and Computational Acoustics
(2025) 2550018 (36 pages)

DOI: 10.1142/S2591728525500185

Propagation of Sound Pulses with Shocks in Fluids: Analytical and Numerical Calculations

E.M. Salomons
TNO Netherlands Organization of Applied Scientific Research
Acoustic Signatures & Noise Control, Oude Waalsdorperweg 63
2597 AK, The Hague, The Netherlands
erik.salomons@tno.nl

Received 5 November 2025
Revised 15 December 2025
Accepted 15 December 2025
Published 10 January 2026

Explosions in fluids generate sound pulses with shocks. In this article, we analyze the effect of the initial waveform on the nonlinear propagation of the sound pulses. We focus on peak pressure, pulse duration, waveform, and sound exposure integrated over the waveform. We use an analytical method based on weak-shock theory and the equal-area rule. For an N wave and an exponential wave, the analytical solutions for peak pressure and pulse duration agree with solutions reported in the literature. For a Friedlander wave, we present a solution that illustrates how analytical solutions for other, more complex, waveforms can be derived. We also describe an efficient numerical method for nonlinear propagation of sound pulses with shocks. Numerical results are in good agreement with analytical results. We use the numerical method to calculate the effect of dissipation. The analytical and numerical solutions are developed for plane, cylindrical, and spherical sound pulses. For sound pulses generated by explosions in water and in air, we compare analytical and numerical results with experimental data and empirical relations from the literature.

Keywords: Explosions in fluids; shock waves; nonlinear propagation.

1. Introduction

To predict and understand the propagation of finite-amplitude sound pulses in fluids, nonlinear deviations from the theory of linear acoustics must be taken into account. Well-known nonlinear propagation phenomena are waveform distortion and shock formation. Waveform distortion originates from the variation of the sound speed with the sound pressure and the fluid velocity, which is neglected in linear acoustics. The formation of shocks in distorted waveforms has been explained by weak-shock theory.[1–3]

Sound pulses with shocks are generated in practice by the detonation of explosives in water or in air. The waveform of the sound pulses has been modeled by various mathematical functions. For explosions in water, an exponential waveform with a leading shock front is a usual approximation.[4–7] The waveform is generally referred to as the 'shock wave', and is characterized by the shock peak pressure, P_{sh}, and the time constant, τ_{sh}, which is a measure of the duration of the shock wave. The time constant is related to the characteristic length of the shock wave, L_{sh}, by the approximate expression $L_{\mathrm{sh}} = c_0\tau_{\mathrm{sh}}$, where c_0 is the linear-acoustics sound speed. For explosions in air, the Friedlander function[8] is a usual approximation of the waveform.[9–11] The Friedlander function consists of a shock wave followed by a weaker negative phase.

The waveform generated by an explosive depends on the properties of the explosive. The most important property is the explosion energy, or equivalently, the explosive mass, W, in kilogram TNT equivalent. The principle of similarity states that waveforms for different values of the explosive mass are related to each other by scaling.[4] The scaling is such that waveforms are equal if length and time are scaled by $W^{1/3}$. The shape of the explosive also has an effect on the sound pressures around the explosive, but this effect is restricted to small distances.[12–15]

In propagation studies, the waveform at a certain distance from the source is used as a starting point. Nonlinear propagation effects cause a change of the waveform with increasing distance from the source. The distance is referred to as range, in this article, and is denoted by symbol r. The nonlinear distortion of the waveform causes a continuous decrease of the shock peak pressure, P_{sh}, and a continuous increase of the time constant, τ_{sh}, with range. The functions $P_{\mathrm{sh}}(r)$ and $\tau_{\mathrm{sh}}(r)$ represent the nonlinear propagation of the sound pulse and these functions are studied in this article.

For the exponential shock wave generated by an underwater explosion, Cole[4] describes a theory developed by Kirkwood and Bethe and presents asymptotic expressions for the functions $P_{\mathrm{sh}}(r)$ and $\tau_{\mathrm{sh}}(r)$ (see also Ref. 7). Rogers[16] presents different expressions for $P_{\mathrm{sh}}(r)$ and $\tau_{\mathrm{sh}}(r)$ for the exponential waveform. He mentions that the Kirkwood-Bethe theory is based on the assumption that the waveform remains exponential during propagation, which is an approximation. For explosions in fluids in general, Pierce[2] approximates the shock wave by a triangular waveform, i.e., the positive phase of an N wave. He develops expressions for $P_{\mathrm{sh}}(r)$ and $\tau_{\mathrm{sh}}(r)$, which differ from the expressions of Rogers and Kirkwood-Bethe for the exponential waveform.

In particular the effect of nonlinear pulse broadening, as represented by the function $\tau_{\mathrm{sh}}(r)$, is considerably larger with the expression of Rogers[16] than with the expression of Pierce.[2] One might think that this difference originates from the difference between the exponential waveform assumed by Rogers and the N waveform assumed by Pierce. In this article, we show that the difference originates primarily from a difference in the definition of the time constant, while the effect of the waveform is much smaller.

In Sec. 3 of this article, analytical expressions for $P_{\mathrm{sh}}(r)$ and $L_{\mathrm{sh}}(r)$ are derived for four different initial-waveform functions. In addition, analytical expressions are derived for the waveform and for an integral over the waveform that is related to the sound exposure level. The expressions provide insight into the phenomenon of nonlinear waveform distortion.

The derivations are based on the theory of nonlinear propagation of sound pulses described in Refs. 1–3. We use an explicit characteristics solution, with shocks derived from the equal-area rule, which follows from weak-shock theory and the Rankine-Hugoniot relations. For the exponential waveform, we recover the result of Rogers[16] for P_{sh} and L_{sh}. For the N waveform, we recover the result of Blackstock[3] for P_{sh} and L_{sh}, and we show that the solution agrees with a different mathematical formulation by Pierce.[2] We also present analytical solutions for a sine waveform and a Friedlander waveform. The solution for the sine wave illustrates the formation of shocks by nonlinear waveform distortion. The solution for the Friedlander wave illustrates how analytical solutions for other, more complex, waveforms can be derived.

In addition, we develop a numerical finite-difference method for calculating the nonlinear propagation of sound pulses with shocks. The method is applicable to arbitrary waveforms. We use the method for numerical verification of the analytical results. We also use the method to investigate the effect of dissipation of acoustic energy in the fluid, which is not taken into account in the analytical solution. The dissipation term in the numerical method is consistent with the Burgers equation for one-dimensional nonlinear dissipative waves.[2,3,17] The numerical method is computationally efficient, as it employs a one-dimensional grid that moves along with the sound pulse.

In Sec. 4 of this article, we compare analytical and numerical calculation results with experimental data for underwater explosions[5,6] and with experimental and numerical data for explosions in air.[9,18–20] The comparison for underwater explosions provides insight into empirical relations[6] for $P_{\mathrm{sh}}(r)$ and $\tau_{\mathrm{sh}}(r)$ that are widely used for underwater explosions. Prediction of sound generated by explosions is important in the field of noise control. Sound generated by underwater explosions may cause harmful effects on fishes[21] and sea mammals such as the harbor porpoise.[22–24] Sound generated by explosions in the atmosphere may cause harmful effects on people, in particular noise annoyance.[11,25–28]

For the analytical and numerical solutions in this article, a distinction is made between plane, cylindrical, and spherical sound pulses. Cylindrical and spherical spreading cause a reduction of the sound pressure, which results in a reduction of nonlinear effects. This reduction does not prevent, however, the formation of shocks, as will be illustrated by an example in Sec. 3.1.

While spherical sound pulses are generated by a point source, cylindrical sound pulses are generated by a line source. A practical example of a nonlinear sound pulse with cylindrical spreading is a sonic boom, generated by a projectile moving at supersonic speed through a fluid.[2,3,28–34] The projectile may be a supersonic aircraft, but supersonic bullets also generate sonic booms. The waveform of a sonic boom can be approximated by an N wave.

Reflections of sound waves are ignored in this article. Therefore, the comparison with experimental data for underwater explosions is for the case of deep water, with the source and the receiver far from the sea bottom and the sea surface. In the case of explosions in shallow water, reflections from the sea bottom and the sea surface have large effects on the sound propagation,[7] including shock-wave superposition and Mach-stem formation.[35,36] It should also be noted that the underwater shock wave is followed in practice by several weaker pulses, including cavitation-closure pulses related to reflections by the sea surface.[4,6,37–40] In the case of sound waves in the atmosphere near the ground, the ground surface has large effects on the sound propagation.[41,42]

Refraction of sound waves by sound-speed gradients in the fluid is also ignored. Consequently, the sound pulses travel along straight ray paths emanating from the source. The theory of nonlinear propagation of sound pulses can also be combined with curved sound rays in a refracting fluid, as described in Refs. 2 and 43.

2. Analytical and Numerical Methods

2.1. *Basic equations*

We consider a plane, cylindrical, or spherical sound pulse. The sound pressure $p(r,t)$ is a function of distance r from the source and time t. We assume that the sound pulse travels in a homogeneous nonmoving fluid.

Following Refs. 1–3, we write

$$p(r,t) = g(\phi)\left(\frac{r_0}{r}\right)^{m/2}, \tag{1}$$

where $g(\phi)$ is the waveform at reference distance r_0, and we use $m = 0, 1, 2$ for plane, cylindrical, and spherical sound pulses, respectively. Parameter ϕ is related to r and t, and we have $\phi = r$ for $t = 0$. We assume that the initial waveform at $t = 0$ is concentrated in a limited range interval around $r = r_0$, so Eq. (1) yields $p(r,0) \approx g(\phi)$. Outside this range interval, the waveform is zero or small.

The waveform function $g(\phi)$ is used to account for the nonlinear waveform distortion, while the factor $(r_0/r)^{m/2}$ represents the geometrical-acoustics effect of cylindrical or spherical spreading of the sound pulse. It is assumed that the two effects are independent of each other. This means that the geometrical spreading is not affected by the nonlinear distortion of the waveform. Pierce[2] describes the approach of Eq. (1) as a "wedding" of geometrical acoustics and the nonlinear theory of plane-wave propagation. Whitham[1] refers to it as a "nonlinearization technique" for diverging waves.

In the linear-acoustics approximation, it is assumed that the sound speed is a constant, c_0, and we have $\phi = r - c_0 t$. The sound pressure (1) with $\phi = r - c_0 t$ satisfies the linear-acoustics wave equation in plane, cylindrical, or spherical coordinates. This is exact for the plane and spherical cases, and a good approximation for the cylindrical case.

For nonlinear wave propagation, the variation of the sound speed with sound pressure p is taken into account. It follows from the theory of nonlinear plane waves[1,2,17] that the waveform function $g(\phi)$ satisfies the nonlinear one-way wave equation

$$\partial_t g + (c+v)\partial_r g = 0, \tag{2}$$

with characteristic speed $c+v$. Here, c is the sound speed and v is the acoustic fluid velocity. The following relation[2,17] is used for the characteristic speed:

$$c + v = c_0 + \frac{\beta}{\rho_0 c_0} p, \tag{3}$$

where c_0 is the ambient sound speed, ρ_0 is the ambient density, and β is the constant of nonlinearity. For the calculations presented in this article, we used the following values: $c_0 = 340\,\text{m/s}$, $\rho_0 = 1.2\,\text{kg/m}^3$, and $\beta = 1.2$ for air and $c_0 = 1500\,\text{m/s}$, $\rho_0 = 1000\,\text{kg/m}^3$, and $\beta = 3.6$ for water.[2,44]

Equation (3) is a basic element of the nonlinear theory of waveform distortion and the weak-shock theory for the formation of shocks.[1–3] Weak-shock theory[1–3] is limited to weak shocks, with shock pressures less than typically[2,16] $0.1\rho_0 c_0^2$. The characteristic speed (3) increases linearly with sound pressure p. The term proportional to p combines two contributions: i) the pressure dependence of sound speed c, and ii) the acoustic fluid velocity, for which the linear-acoustics plane-wave relation $v = p/\rho_0 c_0$ is used as an approximation.

2.2. *Analytical solution*

The nonlinear one-way wave equation (2) for the waveform $g(\phi)$ can be solved analytically with the method of characteristics.[1,2] The initial waveform is $g(\phi)$ with $\phi = r$. Each point of the initial waveform travels with a different speed $c + v$, depending on the initial sound pressure. Consequently, the characteristic lines in the rt plane, represented by $dr/dt = c + v$, are not parallel to each other as in the linear case, but have different slopes. The characteristic speed $c + v$ is given by Eq. (3). It is assumed that Eq. (3) is also valid for diverging waves ($m = 1, 2$), with sound pressure p given by Eq. (1).

Consequently, the slope of the characteristics is given by

$$\frac{dr}{dt} = c_0 + \frac{\beta}{\rho_0 c_0} g(\phi) \left(\frac{r_0}{r}\right)^{m/2}. \tag{4}$$

Integration leads to the following parameter representation of the solution for the sound pressure:

$$p(r,t) = g(\phi) \left(\frac{r_0}{r}\right)^{m/2}, \quad r = \phi + c_0 t + E_m(r,t) g(\phi), \tag{5}$$

where we have introduced the function

$$E_m(r,t) = \begin{cases} \dfrac{\beta t}{\rho_0 c_0} & \text{for } m = 0 \\ 2\dfrac{\beta r_0}{\rho_0 c_0^2} \left(\sqrt{\dfrac{r}{r_0}} - 1\right) & \text{for } m = 1 \\ \dfrac{\beta r_0}{\rho_0 c_0^2} \ln \dfrac{r}{r_0} & \text{for } m = 2. \end{cases} \tag{6}$$

The solution $p(r,t)$ at time t is obtained from the solution $p(r,0)$ at time $t=0$, by letting ϕ run through all values for which $g(\phi)$ is nonzero, and calculating the waveform at time t with the equation $p(r,t)=g(\phi)(r_0/r)^{m/2}$. We use the equal-area rule to eliminate multi-valued sections from the solution, as discussed below and evaluated in Sec. 3.

In the integration of Eq. (4) for the cylindrical and spherical cases, we have neglected terms that are small for $r \gg r_0$. The solution represented by Eqs. (5) and (6) can also be derived with the method based on the age variable for nonlinear diverging waves.[2] The age variable is equal to $c_0^{-1}E_m(r,t)$ for cylindrical and spherical waves. Although the age variable does not have the dimension of time,[43] it is a measure of the time during which nonlinear waveform distortion accumulates along the propagation path. The solution developed by Blackstock[3,45,46] presents a similar distinction between the cases of plane, cylindrical, and spherical waves, based on a coordinate transformation to obtain the cylindrical-wave and spherical-wave solutions from the plane-wave solution.

In Sec. 3, we present analytical solutions for four different mathematical functions for the initial waveform. In all cases, the initial waveform has large sound pressures within a limited range interval around $r=r_0$, and small or zero sound pressures elsewhere. Therefore, we approximate Eq. (5) as follows:

$$p(r,t)=g(\phi)\left(\frac{r_0}{r_{\mathrm{c}}}\right)^{m/2}, \quad r=\phi+c_0t+E_m(r_{\mathrm{c}},t)g(\phi), \tag{7}$$

where $r_{\mathrm{c}}=r_0+c_0t$ is the time-dependent range of initial point r_0 moving with speed c_0. The characteristic representation (7) satisfies $\phi=r$ at $t=0$, since $r_{\mathrm{c}}=r_0$ at $t=0$. By the approximation of r by r_{c} on the right-hand sides, we have obtained an explicit characteristics solution.

The function $E_m(r_{\mathrm{c}},t)$ defined by Eq. (6) is expressed as a function of time for $m=0$ and as a function of range r_{c} for $m=1$ and 2. By using $r_{\mathrm{c}}=r_0+c_0t$, we can express $E_m(r_{\mathrm{c}},t)$ for all three values of m either as a function of time or as a function of range r_{c}. In particular, $E_0(r_{\mathrm{c}},t)$ is equal to $(\beta r_0/\rho_0c_0^2)(r_{\mathrm{c}}/r_0-1)$.

The term $E_m(r_{\mathrm{c}},t)g(\phi)$ in Eq. (7) represents the effect of nonlinear waveform distortion. After a certain time, the solution represented by Eq. (7) becomes multi-valued. A single-valued solution with a pressure discontinuity is obtained by applying the equal-area rule.[1–3] The discontinuity is referred to as 'shock', but we also use the term 'shock front' in this article. In the lossless fluid considered here, the shock front is a discontinuity, but in a fluid with dissipation, the shock front has a finite thickness, as illustrated in Sec. 3.6.

The approximation of r by r_{c} on the right-hand sides of Eq. (7) makes it possible to apply the equal-area rule analytically for the four waveforms considered in Sec. 3. As explained in Sec. 3, the application of the equal-area rule is based on an integral $I=\int p\,dr$ over the waveform, and with the approximation of r by r_{c} on the right-hand sides of Eq. (7), the integral can be evaluated analytically. We note that the difference between the original factor $(r_0/r)^{m/2}$ in Eq. (5) and the factor $(r_0/r_{\mathrm{c}})^{m/2}$ in Eq. (7) is negligible for large r. This is discussed further in Secs. 2.3 and 3.1.

2.3. *Numerical solution*

Substitution of Eqs. (3) and (5) into the nonlinear one-way wave equation (2) gives

$$D_t p = -\frac{m}{2}\frac{c_0 p}{r} - \partial_r\left(\frac{1}{2}\frac{\beta}{\rho_0 c_0}p^2\right) + \delta\partial_r^2 p, \tag{8}$$

where $D_t p = \partial_t p + c_0\partial_r p$ is the total derivative in a frame moving in positive r direction with speed c_0. The first term on the right-hand side represents geometrical spreading, the second term represents nonlinear waveform distortion, and the third term has been included to account for dissipation of acoustic energy in the fluid, which is represented by parameter δ. The third term is consistent with the Burgers equation for one-dimensional nonlinear dissipative waves[2,3,17] and is discussed further in Sec. 3.6. In the derivation of Eq. (8), terms that are second-order in p and that are small at large range have been neglected. The equation can be considered as the one-dimensional formulation of the nonlinear progressive wave equation.[35,47]

We now describe the numerical finite-difference integration of Eq. (8). First, a starting sound pulse $p(r,0)$ is generated, within a limited interval on the r axis. A one-dimensional grid on the r axis is used, with constant grid spacing Δr. The grid moves with speed c_0 in positive r direction. Thus, for all grid points, we replace r by $r + c_0\Delta t$ after each integration time step Δt.

We use a split-step approach, in which each time step consists of the following three partial steps.

Step 1. Solution of the geometrical-spreading part (only for $m = 1, 2$):

$$D_t p = -\frac{m}{2}\frac{c_0 p}{r}. \tag{9}$$

Step 2. Solution of the nonlinear part:

$$D_t p = -\partial_r\left(\frac{1}{2}\frac{\beta}{\rho_0 c_0}p^2\right). \tag{10}$$

Step 3. Solution of the dissipation part:

$$D_t p = \delta\partial_r^2 p. \tag{11}$$

For the solution of Eq. (9), we use a Crank-Nicholson integration scheme. For the small effect of dissipation represented by Eq. (11), we use an explicit integration scheme. For the solution of Eq. (10), we use a hybrid upwind difference scheme described by McDonald and Ambrosiano.[48] The hybrid scheme combines a first-order scheme and a second-order scheme by the method of flux correction.[49] As will be shown in Secs. 3 and 4, this scheme yields good agreement with analytical results. For comparison, we also performed the numerical calculations presented in Secs. 3 and 4 with the first-order scheme. Differences between the results of the first-order scheme and the hybrid scheme are negligible, on the scales of the graphs presented here. If one zooms in on the shock front, however, the hybrid scheme yields a steeper shock front than the first-order scheme does.

The result of the numerical integration is a series of waveforms at discrete range points, for times equal to 0, Δt, $2\Delta t$, etc. To derive the time signals at selected range points, one may choose Δr and Δt such that $\Delta r/(c_0\Delta t)$ is an integer, n, and use every n-th sample for the time signal. One may also use the approximate relation $r = \phi + c_0 t$, i.e., neglect the nonlinear term in Eq. (5), for the conversion from waveform to time signal. This is a good approximation, since the waveform is concentrated in a limited range interval.

In Secs. 3 and 4, we consider waveforms at selected times, and we also consider waveform parameters as a function of time or range. In Sec. 4, we consider the time constant τ_{sh} to represent the duration of the waveform, which we calculate from the length L_{sh} of the waveform with the relation $\tau_{\mathrm{sh}} = L_{\mathrm{sh}}/c_0$.

We note that the variation of the geometrical-acoustics factor $(r_0/r)^{m/2}$ over the narrow waveform is small. The starting waveform for the numerical method is $g(\phi)(r_0/r)^{m/2}$, as in Eq. (5). For the analytical method, the starting waveform is approximated by $g(\phi)(r_0/r_{\mathrm{c}})^{m/2}$, which is $g(\phi)$ since $r_{\mathrm{c}} = r_0$ for $t = 0$. This small difference in initial waveform is eliminated by the propagation, i.e., by a similar difference in the geometrical-spreading factor. This factor is $(r_0/r)^{m/2}$ for the numerical method (represented by the geometrical-spreading term in Eq. (8)), while it is $(r_0/r_{\mathrm{c}})^{m/2}$ for the analytical method. This is illustrated in Sec. 3.1.

For the numerical calculations for water described in Sec. 3, we used a grid spacing of 0.3 cm and a time step varying between 0.1 ms and 0.3 ms. For the calculations for explosions in water described in Sec. 4.1, up to a range of 10 km, we used a grid spacing of 1 cm and a time step of 0.3 ms. For the calculations for explosions in air described in Sec. 4.2, up to a range of 2 km, we used a grid spacing of 3 cm and a time step of 0.3 ms.

For the first example considered in Sec. 3, the maximum sound pressure is 1 MPa, so from Eq. (3) we find a maximum propagation speed of 1502.4 m/s. The time step for this case was 0.3 ms, and the maximum Courant number for the frame moving with speed c_0 is therefore 0.24. For the other cases, the maximum Courant number is also below 0.5.

3. Evaluation for Four Waveforms

In this section, we derive the analytical solutions for four initial-waveform functions: a single period of a sine function (Section 3.1), an N wave function (Section 3.2), an exponential function (Section 3.3), and a Friedlander function (Section 3.4). For the N wave function and the exponential function, we recover results for P_{sh} and L_{sh} from the literature. The solution for the sine function illustrates the development of shocks in a continuous sound pulse. The solution for the Friedlander function demonstrates how analytical solutions can be derived for other, more complex, waveforms.

We illustrate the solutions with examples for plane and spherical sound pulses. We compare the analytical results with numerical results calculated with the finite-difference method described in Sec. 2.3. Dissipation is excluded from the numerical solutions in Secs. 3.1–3.5, since it is not included in the analytical solutions. In Sec. 3.6, we consider the effect of dissipation.

The examples in Secs. 3.1–3.6 are for water. For the sine wave considered in Sec. 3.1, we selected values for waveform parameters P and L such that the results illustrate nonlinear effects over the propagation range of 2 km. For the three waveforms with shocks considered in Secs. 3.2–3.4, we selected values of P and L partly based on empirical values for underwater explosions, as described in Secs. 3.2 and 4.1. In Sec. 3.5, we compare the results for the three waveforms with each other.

3.1. *Sine wave*

We consider a single period of a sine function for the initial waveform:

$$g(\phi) = P \sin\left(\frac{\phi - \phi_0}{L}\pi\right), \quad \text{with } \phi_0 - L \leq \phi \leq \phi_0 + L, \tag{12}$$

where P is the sound pressure amplitude, L is the half wavelength, and ϕ_0 is the central position of the waveform. The waveform is zero outside the indicated ϕ interval.

We consider two examples, a plane pulse and a spherical pulse, with $P = 1000\,\text{kPa}$ and $P = 5000\,\text{kPa}$, respectively. For both pulses, we use $\phi_0 = 20\,\text{m}$ and $L = 1\,\text{m}$. The initial waveforms are illustrated in graphs (a) and (c) of Fig. 1.

At time $t = 0$, we have $r = \phi$, and the end points of the waveform are located at $r_1 = \phi_1 = 19\,\text{m}$ and $r_2 = \phi_2 = 21\,\text{m}$. The central point at $t = 0$ is located at $r_0 = \phi_0$. The sound pressure is zero at this point. At time t, this point has moved to position $r_\text{c} = r_0 + c_0 t$.

With increasing time, the waveform moves along the r axis in positive direction. The distorted waveform is given by Eq. (7). After a certain time, the waveform develops two

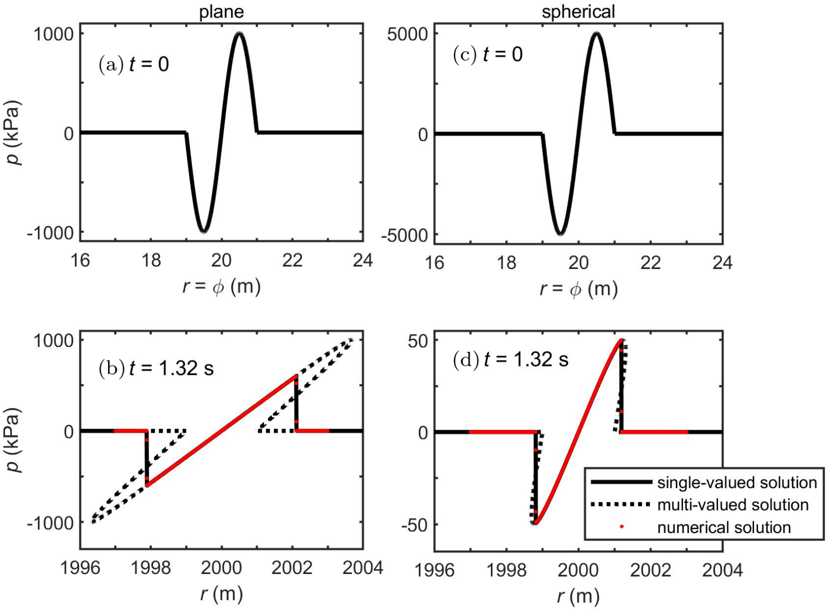

Fig. 1. Plane (a, b) and spherical (c, d) examples of waveforms, for the case of an initial sine waveform ($t = 0$). The waveforms at time 1.32 s are shown in graphs (b) and (d).

multi-valued sections, as illustrated by the dotted lines in graphs (b) and (d) of Fig. 1 for time 1.32 s. We refer to this solution as the multi-valued solution. The central point of zero sound pressure is located at $r_{\mathrm{c}} = 2000\,\mathrm{m}$ at time 1.32 s.

The physical single-valued solution contains two shocks, which replace the multi-valued sections. The single-valued solution at time 1.32 s, calculated with the analytical method described below, is represented by the solid lines in graphs (b) and (d) of Fig. 1. There is good agreement with the numerical solution, represented by the red dots.

As mentioned in Sec. 2.3, there is a small difference between the numerical and analytical waveforms at $t = 0$, for $m = 2$ (spherical case). The waveform at $t = 0$ is $g(\phi)r_0/r$ for the numerical method, while it is $g(\phi)r_0/r_{\mathrm{c}}$ for the analytical method. Consequently, the negative peak at $r = 19.5\,\mathrm{m}$ is 2.5% deeper with the numerical method than with the analytical method, while the positive peak at $r = 20.5\,\mathrm{m}$ is 2.5% lower. This small initial difference is eliminated by the propagation, as explained in Sec. 2.3. The difference is smaller than 1% for $r_{\mathrm{c}} > 50\,\mathrm{m}$.

To calculate the single-valued solution from the multi-valued solution, we have to determine the locations of the two shocks. The shock locations are derived with the equal-area rule,[1–3] which states that the shock cuts the multi-valued section into two parts of equal area. Whitham[1] explains this by the argument that both the multi-valued solution and the single-valued solution must satisfy mass conservation, so $\int \rho \, dr$ must be equal for the two solutions. The equal-area rule can also be derived rigorously from the Rankine-Hugoniot relations for conservation of mass, momentum, and energy at the shock.[2,3] For weak shocks, the Rankine-Hugoniot relations imply that the shock moves with a speed that is the average of the wave speeds just behind and just ahead of the shock, and this leads to the equal-area rule.[2,3]

We consider the multi-valued solution at time t and we will derive an expression for the location r_{sh} of the leading shock, i.e., the shock in the positive phase. For fixed time t, we can consider r as function of ϕ, so we have $r = r(\phi)$. We consider the integral $I = \int p \, dr$ over a part of the positive phase, from a point at location $r(\phi)$ to the end point at location $r(\phi_2)$, with $\phi_2 = \phi_0 + L$. If $r(\phi)$ is equal to the shock location $r_{\mathrm{sh}}(\phi_{\mathrm{sh}})$, then the equal-area rule states that the integral I vanishes. We rewrite the integral I as follows:

$$I = \int_{\phi}^{\phi_2} g(\phi) \left(\frac{r_0}{r_{\mathrm{c}}}\right)^{m/2} \frac{dr}{d\phi} \, d\phi. \tag{13}$$

We use Eqs. (7) and (12) and change the integration variable ϕ in Eq. (13) to the variable $y = \pi(\phi - \phi_0)/L$, which gives $dr/d\phi = 1 + A\cos y$, and we find

$$I = \frac{PL}{\pi} \left(\frac{r_0}{r_{\mathrm{c}}}\right)^{m/2} \left(1 - \frac{A}{4} + \cos y + \frac{A}{4}\cos 2y\right), \tag{14}$$

where A is a dimensionless parameter:

$$A = \frac{P\pi}{L} E_m(r_{\mathrm{c}}, t). \tag{15}$$

The values of y and ϕ at the shock location follow from $I = 0$, which gives

$$y_{\mathrm{sh}} = \arccos\left(1 - \frac{2}{A}\right), \quad \phi_{\mathrm{sh}} = \frac{y_{\mathrm{sh}} L}{\pi} + \phi_0. \tag{16}$$

The corresponding shock location r_{sh} follows from Eq. (7). For the shock location in the negative phase, we obtain from the symmetry $\phi_{\mathrm{sh}} = -(y_{\mathrm{sh}} L/\pi) + \phi_0$, with the value of y_{sh} given in Eq. (16).

Parameter A increases with time. For small times, A is small, and the argument $1 - 2/A$ is smaller than -1, so y_{sh} is undefined and there is no shock. At time t_1 such that $A = 1$, we have $y_{\mathrm{sh}} = \pi$ and the shock develops. At this time, the end point of the sine waveform with $\phi = \phi_2$ has reached a point where the slope dp/dr is infinite. From $A = 1$, we find for the plane case $t_1 = \rho_0 c_0 L/(\beta P \pi)$. For the spherical case, we find the following expressions for time t_1 and the corresponding value $r_{\mathrm{c}} = r_0 + c_0 t_1$, which we denote as r_{c1}:

$$r_{\mathrm{c1}} = r_0 \exp\left(\frac{\rho_0 c_0^2 L}{\beta r_0 P \pi}\right), \quad t_1 = (r_{\mathrm{c1}} - r_0)/c_0. \tag{17}$$

Time t_1 is referred to as shock formation time[50] and distance r_{c1} is referred to as shock formation distance.[3]

The maximum of the sine wave travels with the speed corresponding with $y_{\max} = \frac{1}{2}\pi$. The maximum has reached the shock at a time t_2 where $y_{\mathrm{sh}} = y_{\max}$, corresponding with $A = 2$. For the plane case, we find $t_2 = 2\rho_0 c_0 L/(\beta P \pi)$. For the spherical case, we find the following expressions for time t_2 and the corresponding value $r_{\mathrm{c}} = r_0 + c_0 t_2$, which we denote as r_{c2}:

$$r_{\mathrm{c2}} = r_0 \exp\left(\frac{2\rho_0 c_0^2 L}{\beta r_0 P \pi}\right), \quad t_2 = (r_{\mathrm{c2}} - r_0)/c_0. \tag{18}$$

After time t_1, the distorted sine wave develops shocks in the positive and negative phases. The shock in the positive phase is located at $y = y_{\mathrm{sh}}$ and the shock in the negative phase at $y = -y_{\mathrm{sh}}$. The single-valued solution is given by $p(r) = g(\phi)(r_0/r_{\mathrm{c}})^{m/2}$ for $-y_{\mathrm{sh}} \leq y \leq y_{\mathrm{sh}}$ and $p = 0$ elsewhere. The pressure of the shock front in the positive phase is denoted as P_{sh} and the half wavelength of the distorted sine wave as $L_{\mathrm{sh}} = r_{\mathrm{sh}} - r_{\mathrm{c}}$.

An expression for P_{sh} as a function of range r_{c} follows from $p = g(\phi)(r_0/r_{\mathrm{c}})^{m/2}$ evaluated at ϕ_{sh}, which depends on y_{sh} through Eq. (16). This gives

$$P_{\mathrm{sh}} = P\left(\frac{r_0}{r_{\mathrm{c}}}\right)^{m/2} \sin y_{\mathrm{sh}}. \tag{19}$$

An expression for L_{sh} as a function of range r_{c} follows from Eqs. (7), (15), and (16):

$$L_{\mathrm{sh}} = \frac{L}{\pi}(y_{\mathrm{sh}} + A \sin y_{\mathrm{sh}}). \tag{20}$$

In Eqs. (19) and (20), $\sin y_{\mathrm{sh}}$ can be written as $2A^{-1}\sqrt{A-1}$, as follows from Eq. (16). Equation (19) for P_{sh} agrees with the solution derived by Blackstock.[51]

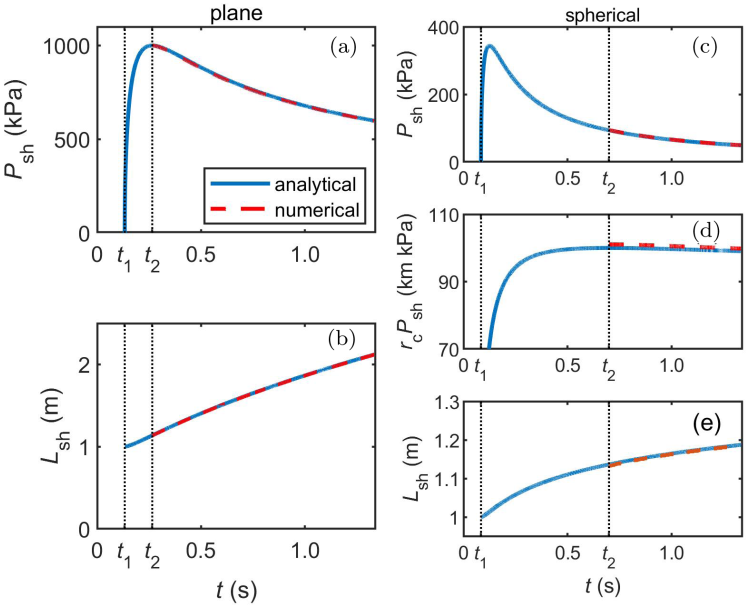

Fig. 2. Shock parameters $P_{\rm sh}$ and $L_{\rm sh}$ as a function of time t. Graphs (a) and (b) are for the plane sine pulse and graphs (c)–(e) are for the spherical sine pulse.

For the plane and spherical examples with the initial waveforms specified above, Fig. 2 shows the variation of $P_{\rm sh}$ and $L_{\rm sh}$ with time t. The blue curves represent the analytical solution, given by Eqs. (19) and (20). The dashed red curves represent the numerical solution. The shock thickness of the numerical solution is about 1.2 cm in this case, and we included a half shock thickness (0.6 cm) in the numerical values for $L_{\rm sh}$, although the effect of this is hardly visible on this scale. The finite thickness of the shock front is caused by numerical dissipation in the numerical solution. There is good agreement between the analytical results and the numerical results.

The two times t_1 and t_2, which were defined above, are indicated in the graphs by vertical dotted lines. For $t < t_1$, the waveform contains no shocks. For $t_1 < t < t_2$, there are gradually increasing shocks, while the shock peak pressure $P_{\rm sh}$ is still lower than the maximum pressure of the waveform. For $t > t_2$, $P_{\rm sh}$ is equal to the maximum pressure of the waveform. In Fig. 2, we show numerical results only for $t > t_2$, for simplicity, as the shocks for $t > t_2$ are easily identified as the points of maximum and minimum sound pressure.

Graph (d) in Fig. 2 shows the product $r_{\rm c}P_{\rm sh}$ as a function of time. Beyond time t_2, the product shows a small decrease with increasing time. This decrease is a consequence of nonlinear waveform distortion, since, in the linear-acoustics approximation, $r_{\rm c}P_{\rm sh}$ would be a constant.

Blackstock[51] notes that, in the limit of large propagation times, the distorted sine wave "resembles an N wave". At the end of this section, we show that the asymptotic waveform for $t \to \infty$ is an N wave. The waveforms shown in Fig. 1 for time 1.32 s do resemble N waves. For the spherical case, however, there is still a small deviation from an N wave visible. The convergence to the asymptotic form is slower for the spherical case than for the plane case, with the parameters used here.

We consider the following integral over the full waveform:

$$I_2 = \int p^2 dr. \tag{21}$$

We refer to I_2 as sound exposure integral, since I_2 is in good approximation equal to the sound exposure $E = \int p^2 dt$ multiplied by sound speed c_0. Here, we use the approximate relation $dr = c_0 dt$, so the wavelength is equal to the period of the pressure-time signal $p(t)$ multiplied by c_0. The sound exposure level (SEL) is given by $L = 10 \lg(E/E_{\mathrm{ref}})$ with reference exposure $E_{\mathrm{ref}} = 10^{-12}$ Pa^{2}s.

To evaluate the integral I_2, we proceed as before for the integral I. We change the integration variable to the variable $y = \pi(\phi - \phi_0)/L$. This gives

$$I_2 = 2 \int_0^{y_{\max}} g^2(\phi) \left(\frac{r_0}{r_{\mathrm{c}}}\right)^m \frac{dr}{d\phi} \frac{d\phi}{dy} dy, \tag{22}$$

where the integration is performed over the positive phase and the factor of 2 accounts for the negative phase. The upper integration limit $y_{\max}$ is equal to π for $t \leq t_1$ and y_{sh} for $t > t_1$. The result is

$$I_2 = \frac{P^2 L}{\pi} \left(\frac{r_0}{r_{\mathrm{c}}}\right)^m \left(y_{\max} - \frac{1}{2} \sin 2y_{\max} + \frac{2}{3} A \sin^3 y_{\max}\right). \tag{23}$$

For $t \leq t_1$, we find $I_2 = P^2 L (r_0/r_{\mathrm{c}})^m$. Consequently, I_2 is a constant for $m = 0$ (plane case) and $r_{\mathrm{c}}^m I_2$ is a constant for $m = 2$ (spherical case). Beyond time t_1, I_2 (plane case) and $r_{\mathrm{c}}^2 I_2$ (spherical case) decrease with time, as shown in Fig. 3. The numerical results agree well with the analytical results calculated with Eq. (23).

In the limit $t \to \infty$, we have $A \to \infty$, $\sin y_{\mathrm{sh}} \to 2/\sqrt{A}$, and $\sin y_{\mathrm{sh}} \to y_{\mathrm{sh}}$. This yields the following asymptotic relations: $P_{\mathrm{sh}} = P(r_0/r_{\mathrm{c}})^{m/2} 2/\sqrt{A}$, $L_{\mathrm{sh}} = 2\sqrt{A} L/\pi$, and $I_2 = \frac{2}{3}(P^2 L/\pi)(r_0/r_{\mathrm{c}})^m 8/\sqrt{A}$. These relations satisfy the N-wave relation $I_2 = \frac{2}{3} P_{\mathrm{sh}}^2 L_{\mathrm{sh}}$. The asymptotic waveform for $t \to \infty$ is an N wave, as it originates from a straight segment of vanishing length around the center point of the sine function, with y ranging from $-y_{\mathrm{sh}}$ to

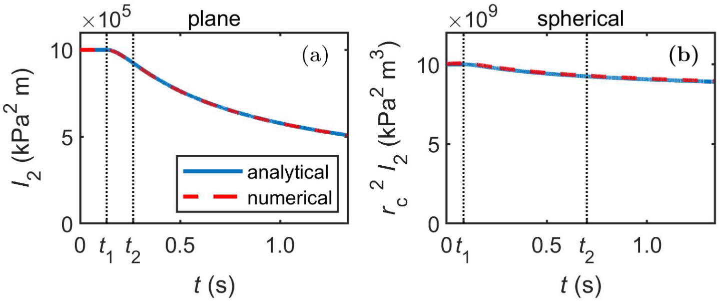

Fig. 3. Sound exposure integral I_2 for the plane sine pulse (a) and product $r_{\mathrm{c}}^2 I_2$ for the spherical sine pulse (b), as a function of time t.

y_{sh}. An N wave is also the asymptotic waveform for other initial waveforms, as demonstrated by Coulouvrat,[52] using a different approach than the approach based on the equal-area rule.

3.2. *N wave*

We consider an N wave for the initial waveform:

$$g(\phi) = P\left(1 + \frac{\phi - \phi_0}{L}\right), \quad \text{with } \phi_0 - 2L \le \phi \le \phi_0, \tag{24}$$

where P is the sound pressure amplitude, L is the half wavelength, and ϕ_0 is the position of the leading shock front. The waveform is zero outside the indicated ϕ interval. The waveform of sonic booms generated by supersonic projectiles can be approximated by an N wave.[2,3,28–33]

We consider two examples, a plane pulse and a spherical pulse, with $P = 1000\,\mathrm{kPa}$ and $P = 5485.6\,\mathrm{kPa}$, respectively. For both pulses, we use $\phi_0 = 20\,\mathrm{m}$ and $L = 0.5844\,\mathrm{m}$. The values of 5485.6 kPa and 0.5844 m were calculated with the Arons-Weston relations for a spherical exponential wave, for 20 kg TNT at a distance of 20 m (see Sec. 4.1). The initial waveforms are illustrated in graphs (a) and (c) of Fig. 4.

The end points of the waveform at time $t = 0$ are located at $r_1 = \phi_0 - 2L = 18.8312\,\mathrm{m}$ and $r_0 = \phi_0 = 20\,\mathrm{m}$. The central point, with zero sound pressure, is located at $r_{\mathrm{z}} = \phi_0 - L$. At time t, the central point has moved to $r_{\mathrm{z}} + c_0 t$, which is equal to $r_{\mathrm{c}} - L$, where $r_{\mathrm{c}} = r_0 + c_0 t$ was introduced in Sec. 2.2. In contrast with the sine wave, the initial N wave already has two

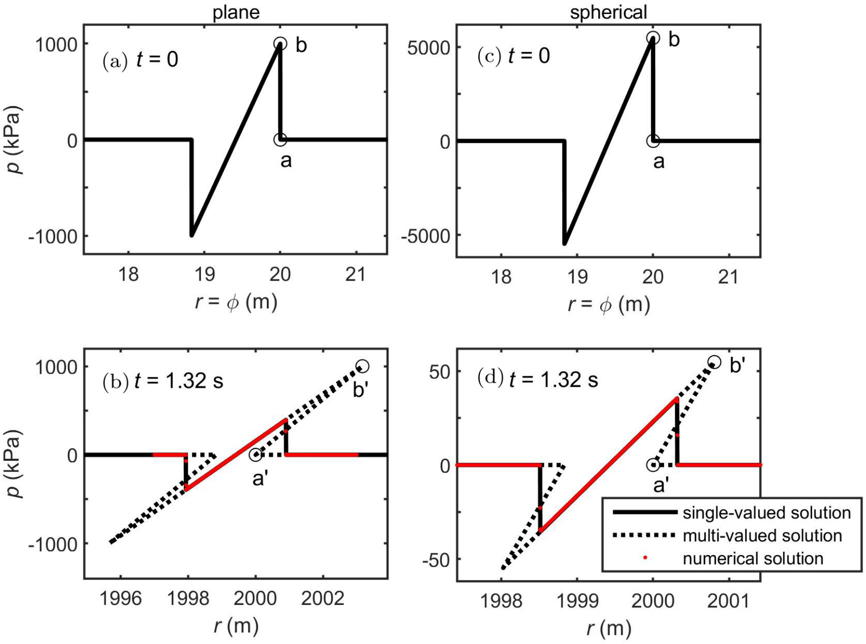

Fig. 4. Plane (a, b) and spherical (c, d) examples of waveforms, for the case of an initial N waveform ($t = 0$). The waveforms at time 1.32 s are shown in graphs (b) and (d).

shocks. Since the propagation speed $c_0 + \beta p/(\rho_0 c_0)$ increases linearly with sound pressure p, the N wave remains an N wave for all times.

The distorted waveform is given by Eq. (7). For all times $t > 0$, the waveform develops two multi-valued sections, as illustrated by the dotted lines in graphs (b) and (d) of Fig. 4 for time 1.32 s. At time 1.32 s, we have $r_\mathrm{c} = 2000\,\mathrm{m}$, and the central point of zero sound pressure is located at range $r_\mathrm{c} - L = 1999.4156\,\mathrm{m}$. The physical single-valued solution contains two shocks, which replace the multi-valued sections. The single-valued solution at time 1.32 s is represented by the solid lines in graphs (b) and (d) of Fig. 4. There is good agreement with the numerical solution, represented by the red dots.

The shock location r_sh at time t in the positive phase is derived from the equal-area rule, as for the sine wave. We consider the integral $I = \int p\, dr$ over a part of the positive phase, from a point at location $r(\phi)$ to the end point at location $r(\phi_0)$. The initial waveform is discontinuous at $\phi = \phi_0$, as the pressure drops from $p = P$ (point b in Fig. 4) to $p = 0$ (point a in Fig. 4). Points a and b move to points a' and b' in the waveform at nonzero time, as illustrated for $t = 1.32\,\mathrm{s}$ in Fig. 4. Therefore, we write the integral I as follows:

$$I = \int_{\phi}^{\phi_0} g(\phi) \left(\frac{r_0}{r_\mathrm{c}}\right)^{m/2} \frac{dr}{d\phi} d\phi + I_\mathrm{sh}, \tag{25}$$

where I_sh is the contribution from segment a'-b', and the integral is performed up to point b'.

The term I_sh is equal to $\int_{r_{\mathrm{b}'}}^{r_{\mathrm{a}'}} p\, dr$, which yields $I_\mathrm{sh} = \frac{1}{2}(r_{\mathrm{a}'} - r_{\mathrm{b}'}) g(\phi_0)(r_0/r_\mathrm{c})^{m/2}$. Using $r_{\mathrm{a}'} = \phi_0 + c_0 t$ and $r_{\mathrm{b}'} = \phi_0 + c_0 t + E_m(r_\mathrm{c}, t) g(\phi_0)$, we find

$$I_\mathrm{sh} = -\frac{1}{2} PLB \left(\frac{r_0}{r_\mathrm{c}}\right)^{m/2}, \tag{26}$$

where B is a dimensionless parameter:

$$B = \frac{P}{L} E_m(r_\mathrm{c}, t). \tag{27}$$

The integral in Eq. (25) can be evaluated by changing to the integration variable $y = 1 + (\phi - \phi_0)/L$, and with $dr/d\phi = 1 + B$, we find

$$I = \frac{1}{2} PL(1 + B) \left(\frac{r_0}{r_\mathrm{c}}\right)^{m/2} (1 - y^2) - \frac{1}{2} PLB \left(\frac{r_0}{r_\mathrm{c}}\right)^{m/2}. \tag{28}$$

The shock location follows from $I = 0$, which gives

$$y_\mathrm{sh} = (1 + B)^{-1/2}, \quad \phi_\mathrm{sh} = y_\mathrm{sh} L + \phi_0 - L. \tag{29}$$

The corresponding shock location r_sh follows from Eq. (7). For the shock location in the negative phase, we obtain from the symmetry $\phi_\mathrm{sh} = -y_\mathrm{sh} L + \phi_0 - L$, with the value of y_sh given in Eq. (29).

The shock in the positive phase is located at $y = y_\mathrm{sh}$ and the shock in the negative phase at $y = -y_\mathrm{sh}$. The single-valued solution is given by $p(r) = g(\phi)(r_0/r_\mathrm{c})^{m/2}$ for $-y_\mathrm{sh} \le y \le y_\mathrm{sh}$ and $p = 0$ elsewhere. This is an N wave for all times. The pressure of the shock front in the positive phase is denoted as P_{sh}, and the half length of the N wave as $L_{\mathrm{sh}} = r_{\mathrm{sh}} - r_{\mathrm{z}}$, where $r_{\mathrm{z}} = r_0 - L + c_0 t$ is the range of the central point of the N wave where the sound pressure is zero.

An expression for P_{sh} as a function of range r_{c} follows from $p = g(\phi)(r_0/r_{\mathrm{c}})^{m/2}$ evaluated at ϕ_{sh}, which depends on y_{sh} through Eq. (29). This gives

$$P_{\mathrm{sh}} = P \left(\frac{r_0}{r_{\mathrm{c}}}\right)^{m/2} (1+B)^{-1/2}. \tag{30}$$

An expression for L_{sh} as a function of range r_{c} follows from Eqs. (7), (27), and (29):

$$L_{\mathrm{sh}} = L(1+B)^{1/2}. \tag{31}$$

For the plane and spherical examples with the initial waveforms specified above, Fig. 5 shows the variation of P_{sh} and L_{sh} with time t. The blue curves represent Eqs. (30) and (31). The dashed red curves represent the numerical solution. As for the sine wave, we included a half shock thickness (0.6 cm) in the numerical values for L_{sh}, although the effect of this is hardly visible on this scale. There is good agreement between the analytical results and the numerical results.

Graph (d) in Fig. 5 shows the product $r_{\mathrm{c}} P_{\mathrm{sh}}$. The variation with time of this product is a consequence of nonlinear waveform distortion,

It is of interest to compare Eqs. (30) and (31) for P_{sh} and L_{sh} with the analytical solution of Pierce[2] for spherical N waves. Pierce presents expressions for shock pressure P_{sh} and positive-phase duration T_{sh} of a spherical N wave as a function of range r (Equation 11-9.8

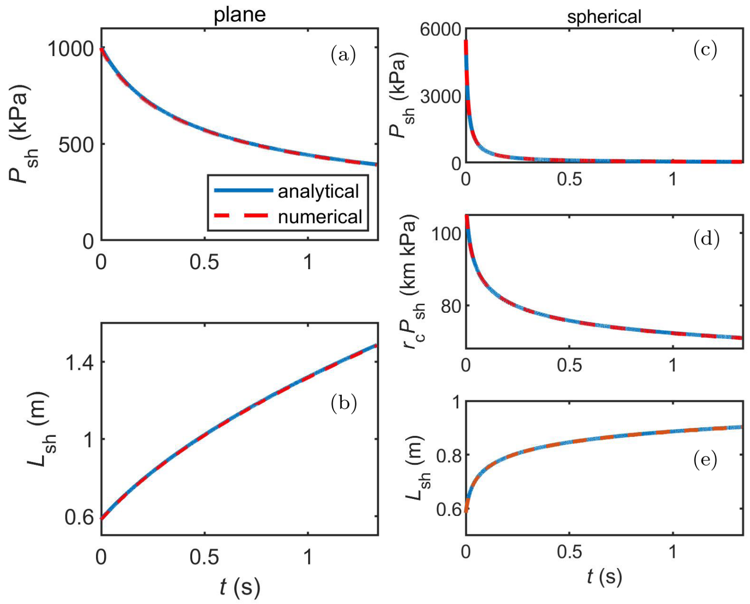

Fig. 5. Shock parameters P_{sh} and L_{sh} as a function of time t. Graphs (a) and (b) are for the plane N wave and graphs (c)–(e) are for the spherical N wave.

in Ref. 2), with two parameters, r^* and K. If we evaluate these parameters for $r = r_0$ and use $L_{\mathrm{sh}} = c_0 T_{\mathrm{sh}}$, then the resulting expressions for P_{sh} and L_{sh} are identical to Eqs. (30) and (31). For numerical evaluation, the expressions (30) and (31) differ from the expressions of Pierce, as parameter r^* decreases exponentially with decreasing P and becomes small for weak shock waves.

Blackstock[3,46] also presents analytical solutions for plane, cylindrical, and spherical N waves. The expressions presented by Blackstock agree with Eqs. (30) and (31). The agreement for plane waves follows from $r_{\mathrm{c}} \approx c_0 t$ for $r_{\mathrm{c}} \gg r_0$. For cylindrical and spherical waves, the agreement is exact.

To evaluate the integral I_2 defined in Eq. (21), we proceed as before for the integral I. We change the integration variable to the variable $y = 1 + (\phi - \phi_0)/L$. The integral is equal to

$$I_2 = 2 \int_0^{y_{\mathrm{sh}}} g^2(\phi) \left(\frac{r_0}{r_{\mathrm{c}}}\right)^m \frac{dr}{d\phi} \frac{d\phi}{dy} dy, \tag{32}$$

where the integration is performed over the positive phase up to the shock front and the factor of 2 accounts for the negative phase. The result is

$$I_2 = \frac{2}{3} P^2 L \left(\frac{r_0}{r_{\mathrm{c}}}\right)^m (1 + B)^{-1/2}. \tag{33}$$

This can also be written as

$$I_2 = \frac{2}{3} P_{sh}^2 L_{sh}. \tag{34}$$

Since this expression can also be obtained by integration of an N wave with amplitude P_{sh} and half wavelength L_{sh}, we have an indirect confirmation that the initial N waveform remains an N wave for all times.

The product $r_{\mathrm{c}}^m I_2$ decreases with time, as shown in Fig. 6. The numerical results agree well with the analytical results calculated with Eq. (33). Figure 6 also includes the results for the exponential and Friedlander waves, which are described in Secs. 3.3 and 3.4.

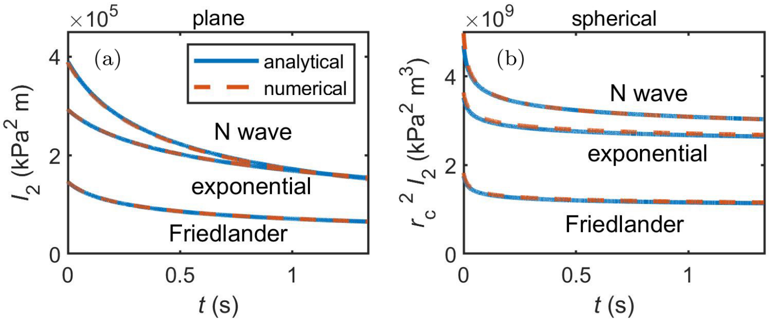

Fig. 6. Sound exposure integral I_2 for the plane case (a) and product $r_{\mathrm{c}}^2 I_2$ for the spherical case (b), as a function of time t, for the examples with an N wave, exponential wave, and Friedlander wave.

3.3. *Exponential wave*

We consider an exponential function for the initial waveform:

$$g(\phi) = P \exp\left(\frac{\phi - \phi_0}{L}\right), \quad \text{with } -\infty < \phi \leq \phi_0, \tag{35}$$

where P is the sound pressure amplitude, L is the relaxation length, and ϕ_0 is the position of the shock front. The waveform is zero outside the indicated ϕ interval. The exponential waveform has been widely used to model the shock wave generated by underwater explosions.[4–7]

We consider two examples, a plane pulse and a spherical pulse, with $P = 1000\,\text{kPa}$ and $P = 5485.6\,\text{kPa}$, respectively. For both pulses, we use $\phi_0 = 20\,\text{m}$ and $L = 0.5844\,\text{m}$. The values of 5485.6 kPa and 0.5844 m are equal to the values used in Sec. 3.2 for the spherical N wave, and were calculated with the Arons-Weston relations for a spherical exponential wave, for 20 kg TNT at a distance of 20 m (see Sec. 4.1). The initial waveform is illustrated in graphs (a) and (c) of Fig. 7. At time $t = 0$, the shock front is located at $r_0 = \phi_0$. In contrast with the N wave, the exponential wave does not remain exponential for all times.

The distorted waveform is given by Eq. (7). For all times $t > 0$, the waveform develops a multi-valued section, as illustrated by the dotted lines in graphs (b) and (d) of Fig. 7 for time 1.32 s. The physical single-valued solution contains a shock, which replaces the

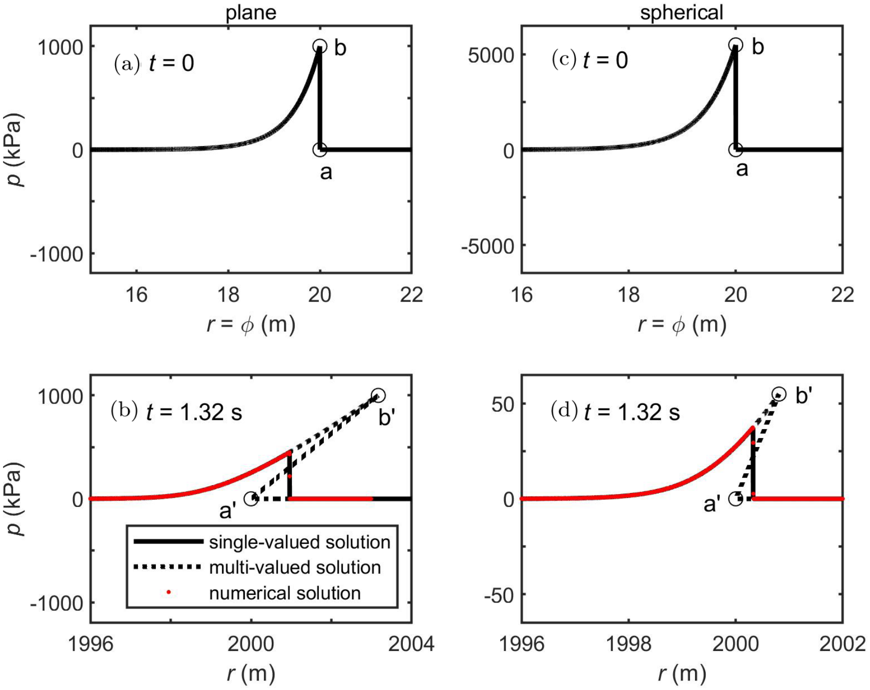

Fig. 7. Plane (a, b) and spherical (c, d) examples of waveforms, for the case of an initial exponential waveform ($t = 0$). The waveforms at time 1.32 s are shown in graphs (b) and (d).

multi-valued section. The single-valued solution at time 1.32 s is represented by the solid lines in graphs (b) and (d) of Fig. 7. There is good agreement with the numerical solution, represented by the red dots.

The shock location r_{sh} at time t is derived from the equal-area rule, as for the sine wave and the N wave. We consider the integral $I = \int p\,dr$ over a part of the waveform, from a point at location $r(\phi)$ to the end point at location $r(\phi_0)$. The initial waveform is discontinuous at $\phi = \phi_0$, as the pressure drops from $p = P$ (point b in Fig. 7) to $p = 0$ (point a in Fig. 7). Points a and b move to points a' and b' in the waveform at nonzero time, as illustrated for $t = 1.32$ s in Fig. 7. Therefore, we write the integral I as follows:

$$I = \int_{\phi}^{\phi_0} g(\phi) \left(\frac{r_0}{r_{\mathrm{c}}}\right)^{m/2} \frac{dr}{d\phi} d\phi + I_{\mathrm{sh}}, \tag{36}$$

where I_{sh} is the contribution from segment a'-b', and the integral is performed up to point b'. In the same way as for the N wave, the term I_{sh} is given by Eq. (26), with parameter B given by Eq. (27). The integral in Eq. (36) can be evaluated by changing to the integration variable $y = (\phi - \phi_0)/L$, which gives $dr/d\phi = 1 + B\mathrm{e}^{y}$, and we find

$$I = PL \left(\frac{r_0}{r_{\mathrm{c}}}\right)^{m/2} \left(1 - \mathrm{e}^{y} - \frac{1}{2} B \mathrm{e}^{2y}\right). \tag{37}$$

The shock location follows from $I = 0$, which gives

$$y_{\mathrm{sh}} = \ln\left(\frac{-1 + \sqrt{1 + 2B}}{B}\right), \quad \phi_{\mathrm{sh}} = y_{\mathrm{sh}} L + \phi_0. \tag{38}$$

The corresponding shock location r_{sh} follows from Eq. (7). We note that for $t = 0$ we have $B = 0$ and $y_{\mathrm{sh}} = 0$. Parameter y_{sh} is the value of y at the shock location. The single-valued solution is given by $p(r) = g(\phi)(r_0/r_{\mathrm{c}})^{m/2}$ for $-\infty < y \leq y_{\mathrm{sh}}$ and $p = 0$ elsewhere.

An expression for P_{sh} as a function of range r_{c} follows from $p = g(\phi)(r_0/r_{\mathrm{c}})^{m/2}$ evaluated at ϕ_{sh}, which depends on y_{sh} through Eq. (38). This gives

$$P_{\mathrm{sh}} = P \left(\frac{r_0}{r_{\mathrm{c}}}\right)^{m/2} \exp y_{\mathrm{sh}}. \tag{39}$$

We define a measure L_{sh} of the length of the shock wave, from the slope of the waveform evaluated at the shock front:

$$L_{\mathrm{sh}} = \left(\frac{d \ln p(r)}{dr}\right)_{\mathrm{sh}}^{-1}. \tag{40}$$

From $p = P(r_0/r_{\mathrm{c}})^{m/2} \exp((\phi - \phi_0)/L)$ we get

$$\frac{d \ln p(r)}{dr} = \frac{1}{L} \frac{d\phi}{dr}. \tag{41}$$

With $d\phi/dr = [1 + B \exp((\phi - \phi_0)/L)]^{-1}$, we find

$$\left(\frac{d \ln p(r)}{dr}\right)^{-1} = L \left[1 + B \exp\left(\frac{\phi - \phi_0}{L}\right)\right]. \tag{42}$$

At the shock front, we have $\phi_{\rm sh} = y_{\rm sh}L + \phi_0$, and we get

$$L_{\rm sh} = L\sqrt{1+2B}. \tag{43}$$

Equations (39) and (43) for $P_{\rm sh}$ and $L_{\rm sh}$ agree with the expressions given by Rogers,[16] who used a different approach for the derivation than the approach based on the equal-area rule. As a comment on the article of Rogers, Persson[53] presented a derivation of the expressions from relations developed by Whitham.

We also consider an alternative measure $L'_{\rm sh}$ of the length of the shock wave: the distance from the shock front at range $r_{\rm sh}$ to the point at range $r_{\rm e}$ where the sound pressure has decreased from $P_{\rm sh}$ to $P_{\rm sh}\exp(-1)$. Thus, $L'_{\rm sh}$ is given by

$$L'_{\rm sh} = r_{\rm sh} - r_{\rm e}. \tag{44}$$

The value of $r_{\rm e}$ is

$$r_{\rm e} = \phi_{\rm sh} - L + c_0 t + BL\exp(y_{\rm sh} - 1). \tag{45}$$

This leads to

$$L'_{\rm sh} = L\left[1 + (-1+\sqrt{1+2B})(1-\exp(-1))\right]. \tag{46}$$

Equations (39) and (46) for $P_{\rm sh}$ and $L'_{\rm sh}$ agree with the expressions given by Blackstock *et al.*[3]

For the plane and spherical examples with the initial waveforms specified above, Fig. 8 shows the variation of $P_{\rm sh}$, $L_{\rm sh}$, and $L'_{\rm sh}$ with time t. Graph (e) shows the product $r_{\rm c}P_{\rm sh}$.

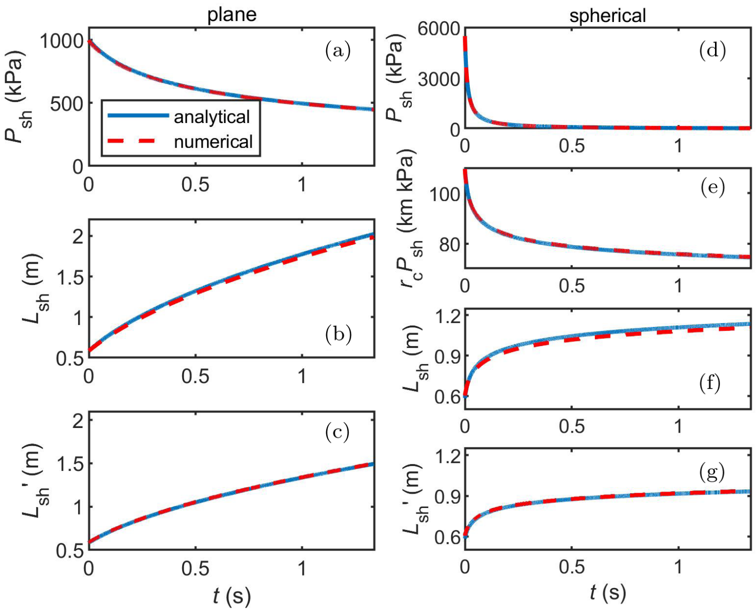

Fig. 8. Shock parameters $P_{\rm sh}$, $L_{\rm sh}$, and $L'_{\rm sh}$ as a function of time t. Graphs (a)–(c) are for the plane exponential wave and graphs (d)–(g) are for the spherical exponential wave.

The blue curves represent Eqs. (39), (43), and (46). The dashed red curves represent the numerical solution. There is good agreement between the analytical results and the numerical results.

As for the sine wave and the N wave, we included a half shock thickness (0.6 cm) in the numerical values for L'_{sh}, although the effect of this is hardly visible on this scale. The shock thickness is not included in the numerical values of L_{sh}. These values were obtained from the numerical waveform, taking the finite-difference slope over a range interval of 0.03 m.

At time zero, L_{sh} and L'_{sh} are equal to L. With increasing time, L_{sh} becomes considerably larger than L'_{sh}. This is an indication that, for nonzero times, the waveform deviates from the exponential form. If the waveform would remain exponential, then L_{sh} and L'_{sh} would be equal for all times.

Comparison with Fig. 5 for the N wave shows that the values of L'_{sh} for the exponential waveform are closer to the values for the N wave than the values of L_{sh} are. This will be analyzed further in Sec. 3.5.

To evaluate the integral I_2 defined in Eq. (21), we proceed as before for the integral I. We change the integration variable to the variable $y = (\phi - \phi_0)/L$. The integral is equal to

$$I_2 = \int_{-\infty}^{y_{\mathrm{sh}}} g^2(\phi) \left(\frac{r_0}{r_{\mathrm{c}}}\right)^m \frac{dr}{d\phi}\frac{d\phi}{dy} dy, \tag{47}$$

where the integration is performed up to the shock front. The result is

$$I_2 = P^2 L \left(\frac{r_0}{r_{\mathrm{c}}}\right)^m \left(\frac{1}{2}\exp^2 y_{\mathrm{sh}} + \frac{1}{3} B \exp^3 y_{\mathrm{sh}}\right). \tag{48}$$

For time zero, this reduces to $I_2 = \frac{1}{2} P^2 L (r_0/r_{\mathrm{c}})^m$. For nonzero time, the result (48) differs from the result $I_2 = \frac{1}{2} P_{\mathrm{sh}}^2 L_{\mathrm{sh}}$ for an exponential waveform (35) with $P = P_{\mathrm{sh}}$ and $L = L_{\mathrm{sh}}$. The difference is smaller if one uses L'_{sh} instead of L_{sh}, but it is still nonzero. This indicates that the exponential waveform does not remain exponential.

The product $r_{\mathrm{c}}^m I_2$ decreases with time, as shown in Fig. 6. The numerical results agree well with the analytical results calculated with Eq. (48).

3.4. *Friedlander wave*

We consider a Friedlander function for the initial waveform:

$$g(\phi) = P\left(1 + \frac{\phi - \phi_0}{L}\right) \exp\left(\frac{\phi - \phi_0}{L}\right), \quad \text{with } -\infty < \phi \le \phi_0, \tag{49}$$

where P is the sound pressure amplitude, L is the relaxation length of the exponential factor, and ϕ_0 is the position of the shock front. At $\phi = \phi_0 - L$, we have $g(\phi) = 0$. The waveform is zero outside the indicated ϕ interval. The Friedlander function[8] has been used to model the waveform generated by explosions in air.[9–11]

We consider two examples, a plane pulse and a spherical pulse, with $P = 1000$ kPa and $P = 5485.6$ kPa, respectively. For both pulses, we use $\phi_0 = 20$ m and $L = 0.5844$ m. The initial waveform is illustrated in graphs (a) and (c) of Fig. 9. At time $t = 0$, the shock front

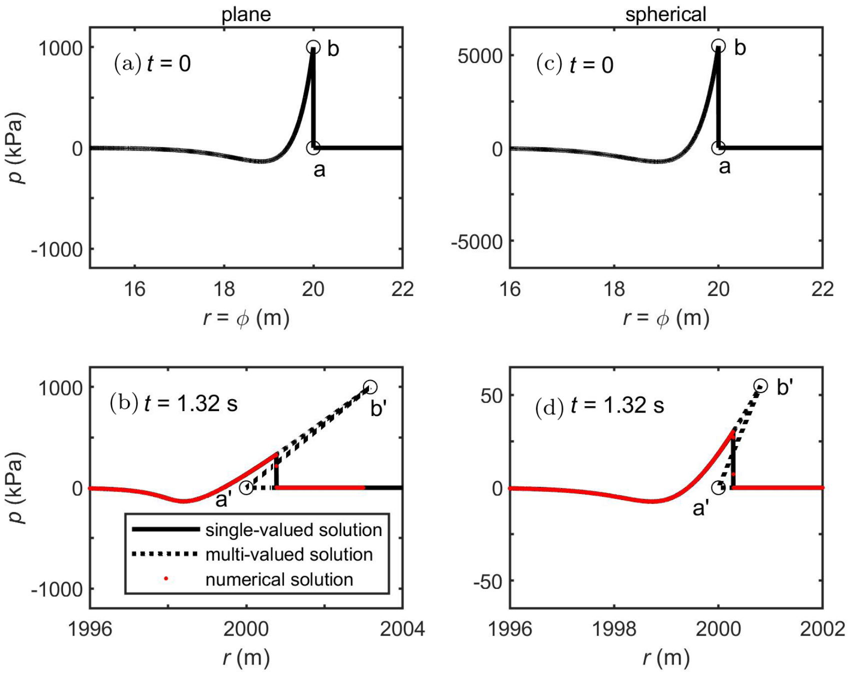

Fig. 9. Plane (a, b) and spherical (c, d) examples of waveforms, for the case of an initial Friedlander waveform ($t = 0$). The waveforms at time 1.32 s are shown in graphs (b) and (d).

is located at $r_0 = \phi_0$. In contrast with the N wave, the Friedlander wave does not remain a Friedlander wave for all times.

The distorted waveform is given by Eq. (7). For all times $t > 0$, the waveform develops a multi-valued section, as illustrated by the dotted lines in graphs (b) and (d) of Fig. 9 for time 1.32 s. The physical single-valued solution contains a shock, which replaces the multi-valued section. The single-valued solution at time 1.32 s is represented by the solid lines in graphs (b) and (d) of Fig. 9. There is good agreement with the numerical solution, represented by the red dots.

The shock location r_{sh} at time t is derived from the equal-area rule, as for the other waveforms. We consider the integral $\int p\, dr$ over a part of the waveform, from a point at location $r(\phi)$ to the end point at location $r(\phi_0)$. The initial waveform is discontinuous at $\phi = \phi_0$, as the pressure drops from $p = P$ (point b in Fig. 9) to $p = 0$ (point a in Fig. 9). Points a and b move to points a' and b' in the waveform at nonzero time, as illustrated for $t = 1.32$ s in Fig. 9. Therefore, we write the integral I as follows:

$$I = \int_{\phi}^{\phi_0} g(\phi) \left(\frac{r_0}{r_{\mathrm{c}}}\right)^{m/2} \frac{dr}{d\phi} d\phi + I_{\mathrm{sh}}, \tag{50}$$

where I_{sh} is the contribution from segment a'-b', and the integral is performed up to point b'. In the same way as for the N wave, the term I_{sh} is given by Eq. (26), with parameter B given by Eq. (27). The integral in Eq. (50) can be evaluated by changing to the integration variable $y = (\phi - \phi_0)/L$, which gives $dr/d\phi = 1 + B(2+y)\mathrm{e}^y$, and we find

$$I = -PL\left(\frac{r_0}{r_\mathrm{c}}\right)^{m/2}\mathrm{e}^y\left(y + \frac{1}{2}B(y^2+2y+1)\mathrm{e}^y\right). \tag{51}$$

The shock location follows from $I(y) = 0$. We solve the equation iteratively with the Newton-Raphson method, and denote the solution as

$$y = y_\mathrm{sh}, \quad \phi_\mathrm{sh} = y_\mathrm{sh}L + \phi_0. \tag{52}$$

The corresponding shock location r_sh follows from Eq. (7). Parameter y_sh is the value of y at the shock location. The single-valued solution is given by $p(r) = g(\phi)(r_0/r_\mathrm{c})^{m/2}$ for $-\infty < y \leq y_\mathrm{sh}$ and $p = 0$ elsewhere.

The iterative solution introduces a numerical element in the analytical solution. For other waveforms than the Friedlander wave, the analytical solution can be obtained in a similar way. In general, for complex waveforms, the integral I as a function of y can be evaluated numerically by a cumulative summation over a densely-spaced set of values of ϕ, so that a numerical solution of $I(y) = 0$ can be obtained.

An expression for P_sh as a function of range r_c follows from $p = g(\phi)(r_0/r_\mathrm{c})^{m/2}$ evaluated at ϕ_sh, which depends on y_sh through Eq. (52). This gives

$$P_\mathrm{sh} = P\left(\frac{r_0}{r_\mathrm{c}}\right)^{m/2}(1+y_\mathrm{sh})\exp y_\mathrm{sh}. \tag{53}$$

We define a measure L_sh of the length of the shock wave as the distance from the shock front at range r_sh to the point at range $r_\mathrm{z} = r_0 - L + c_0 t$ where the sound pressure is zero:

$$L_\mathrm{sh} = r_\mathrm{sh} - r_\mathrm{z}. \tag{54}$$

Using Eq. (7), we find

$$L_\mathrm{sh} = L + \phi_\mathrm{sh} - \phi_0 + E_m(r_\mathrm{c}, t)g(\phi_\mathrm{sh}). \tag{55}$$

For the plane and spherical examples with the initial waveforms specified above, Fig. 10 shows the variation of P_sh and L_sh with time t. Graph (d) shows the product $r_\mathrm{c}P_\mathrm{sh}$. The blue curves represent Eqs. (53) and (55). The dashed red curves represent the numerical solution. Again, we included a half shock thickness (0.6 cm) in the numerical values for L_sh, although the effect of this is hardly visible on this scale. There is good agreement between the analytical results and the numerical results.

To evaluate the integral I_2 defined in Eq. (21), we proceed as before for the integral I. We change the integration variable to the variable $y = (\phi - \phi_0)/L$. The integral is equal to

$$I_2 = \int_{-\infty}^{y_\mathrm{sh}} g^2(\phi)\left(\frac{r_0}{r_\mathrm{c}}\right)^m \frac{dr}{d\phi}\frac{d\phi}{dy}dy, \tag{56}$$

where the integration is performed up to the shock front. The result is

$$I_2 = P^2L\left(\frac{r_0}{r_\mathrm{c}}\right)^m\left[\mathrm{e}^{2y_\mathrm{sh}}\left(\frac{1}{2}y_\mathrm{sh}^2 + \frac{1}{2}y_\mathrm{sh} + \frac{1}{4}\right) + B\mathrm{e}^{3y_\mathrm{sh}}\left(\frac{1}{3}y_\mathrm{sh}^3 + y_\mathrm{sh}^2 + y_\mathrm{sh} + \frac{1}{3}\right)\right]. \tag{57}$$

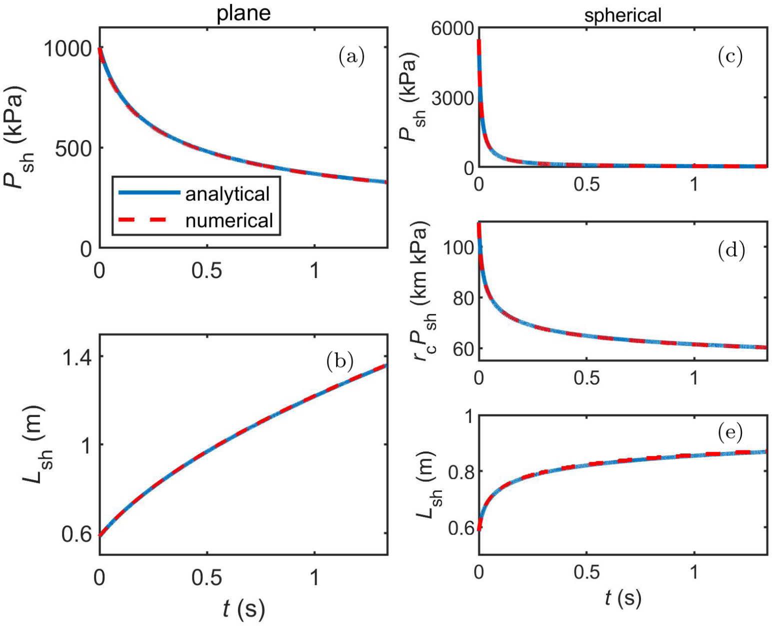

Fig. 10. Shock parameters $P_{\rm sh}$ and $L_{\rm sh}$ as a function of time t. Graphs (a) and (b) are for the plane Friedlander wave and graphs (c)–(e) are for the spherical Friedlander wave.

For time zero, this reduces to $I_2 = \frac{1}{4}P^2L(r_0/r_{\rm c})^m$. For nonzero time, the result (57) differs from the result $I_2 = \frac{1}{4}P_{\rm sh}^2L_{\rm sh}$ for a Friedlander waveform (49) with $P = P_{\rm sh}$ and $L = L_{\rm sh}$. This indicates that the Friedlander waveform does not remain a Friedlander.

The product $r_{\rm c}^mI_2$ decreases with time, as shown in Fig. 6. The numerical results agree well with the analytical results calculated with Eq. (57).

3.5. *Comparison between waveforms*

In this section, we present a comparison of analytical results for the N wave, the exponential wave, and the Friedlander wave. The comparison is for spherical sound pulses. The values of parameters P, L, and ϕ_0 for the three waveforms are 5485.6 kPa, 0.5844 m, and 20 m, respectively, as in Secs. 3.2–3.4.

Figure 11 shows the three waveforms at time $t = 0$ and time $t = 1.32$ s. At time $t = 0$, the shock fronts of the three waveforms are located at range 20 m. At time $t = 1.32$ s, the shock fronts are located at slightly different positions near range 2000 m. Graph (c) is a zoomed-in version of graph (b) for $t = 1.32$ s, showing the differences between the waveforms around the shock front. The exponential wave has the highest peak pressure and the Friedlander wave has the lowest peak pressure. Consequently, the nonlinear pulse broadening is largest for the exponential wave and smallest for the Friedlander wave, leading to the slightly different positions of the shock front, as shown in the graph.

These observations are confirmed by Fig. 12, which shows values of $r_{\rm c}P_{\rm sh}$ and $L_{\rm sh}$ as a function of range $r_{\rm c}$, for the three waveforms. The differences in graph (a) at range

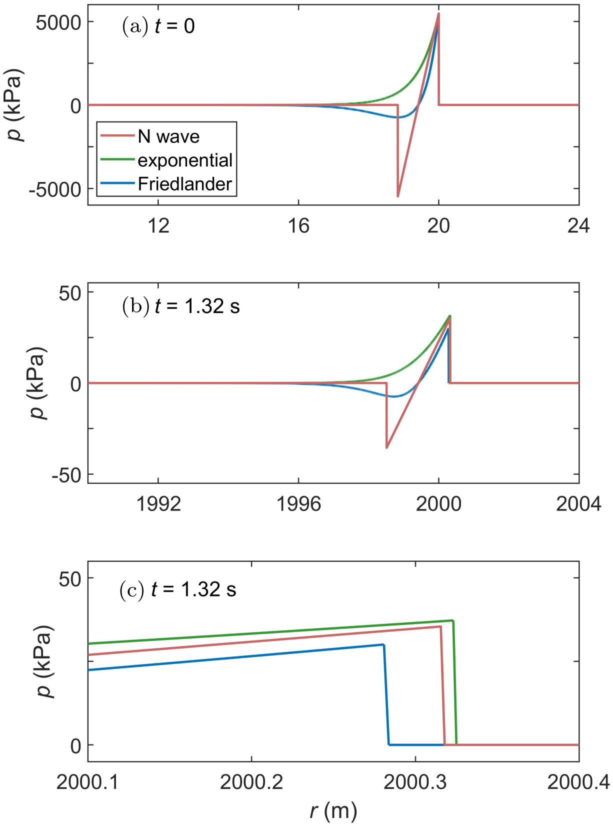

Fig. 11. Waveforms $p(r)$ at time $t = 0$ and time $t = 1.32\,\text{s}$, for the N wave, the exponential wave, and the Friedlander wave.

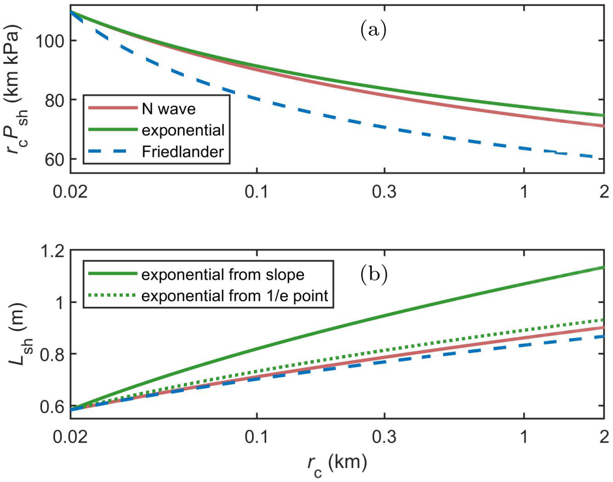

Fig. 12. Values of $r_{\text{sh}}P_{\text{sh}}$ (a) and L_{sh} (b) as a function of range r_{c}, for the N wave, the exponential wave, and the Friedlander wave.

2 km correspond with the differences in shock pressure shown in Fig. 11(c). As indicated in Sec. 3.1, the decrease of the product $r_\mathrm{c}P_\mathrm{sh}$ with range is a consequence of nonlinear waveform distortion, as the product is constant in the linear-acoustics approximation. In graph (b) we have included the two values of L_sh for the exponential waveform defined in Sec. 3.3 (the value derived from the 1/e point was denoted as L'_sh in Sec. 3.3). The graph shows that the value derived from the 1/e point is closer to the values for the N wave and the Friedlander wave than the value derived from the slope is.

Graph (a) of Fig. 12 shows that the values of P_sh for the exponential wave are higher than the values for the N wave, while the values for the Friedlander wave are lower. This can be related to the shapes of the waveforms just behind the shock front. The initial waveforms are given by Eqs. (24), (35), and (49), and are illustrated in Fig. 11(a). For the initial N wave, the slope is constant and equal to P/L. For the initial exponential wave, the slope at the shock front is also equal to P/L, and it is smaller than P/L in the region behind the shock front. For the initial Friedlander wave, the slope at the shock front is equal to $2P/L$, so it is larger than P/L in the region just behind the shock front. With increasing time, the waveforms distort, but the slopes just behind the shock front remain in the same order: smallest for the exponential wave and largest for the Friedlander wave. The slope differences are small, however, and hardly visible in Fig. 11(c).

The slope P/L appears as a factor in parameter B given by Eq. (27). Equation (30) for the N wave shows that the decrease of P_sh with range is larger if the slope P/L is larger. This effect of the slope explains why the decrease of the shock pressure with range is largest for the Friedlander wave and smallest for the exponential wave, as shown in Fig. 12(a). Alternatively, it can be explained by a graphical construction of the shock front from the equal-area rule.

3.6. *Effect of dissipation*

In this section, we consider the effect on the waveform of dissipation of acoustic energy in the fluid. The dissipation was represented by the dissipation term in Eq. (8) for the numerical method.

Parameter δ in the dissipation term in Eq. (8) is related to volume absorption coefficient α, expressed in Nepers per meter. For propagation in water[2,54] and in air,[2,55] coefficient α applies to constant-frequency sound waves and is a function of the fluid properties and the sound frequency. To derive the relation between δ and α, we consider the linear-acoustics one-dimensional wave equation

$$\partial_t p + c_0 \partial_r p = 0, \tag{58}$$

which has the following complex solution in the frequency domain:

$$p(r,t) = p_0 \exp(ikr - i\omega t), \tag{59}$$

where p_0 is the amplitude, $k = \omega/c_0$ is the wave number, and $\omega = 2\pi f$ is the angular frequency corresponding with frequency f. If we include the dissipation term $\delta\partial_r^2 p$ on the right-hand side of Eq. (58), then the solution becomes[17]

$$p(r,t) = p_0 \exp(ikr - i\omega t)\exp(-k^2\delta r/c_0), \tag{60}$$

if we neglect terms quadratic in δ. We identify the second exponential factor with absorption factor $\exp(-\alpha r)$, so we get

$$\alpha = \delta k^2/c_0. \tag{61}$$

We note that α in Nepers per meter is related to α_{dB} in dB per meter by $\alpha_{\mathrm{dB}} = \alpha 20\lg(\mathrm{e})$.

For nonlinear sound pulses, we use Eq. (8) in the time domain. The dissipation term with parameter δ correspond with an absorption coefficient α that is proportional to the square of the frequency, as shown by Eq. (61). Both for water and for air, the variation of α with frequency is more complex than quadratic, so the dissipation term in Eq. (8) yields only a limited representation of the frequency-dependent absorption. We note that a more accurate formulation of the dissipation term for air is presented in Ref. 56.

As an example, we have repeated the calculations for the spherical N wave considered in Sec. 3.2, but now including the effect of dissipation. We have used the formulas from Ref. 54 to calculate $\alpha(f_{\mathrm{ref}})$ at a reference frequency f_{ref}. The corresponding value of δ follows from Eq. (61). We have considered two values for f_{ref}, 500 Hz and 2 kHz. We have α (500 Hz) $= 3.23 \times 10^{-6}$ Np/m and α (2 kHz) $= 1.55 \times 10^{-5}$ Np/m. These values differ by a factor of 4.8, which is smaller than the squared frequency ratio of 16. This illustrates that $\alpha(f)$ is not a quadratic function of frequency.

Figure 13 shows waveforms calculated with the numerical method for time $t = 1.32$ s. Graph (a) shows the linear waveform, calculated without the nonlinear term in Eq. (8), and graph (c) shows the nonlinear waveform. Graphs (b) and (d) zoom in on the leading shock. The effect of dissipation, or absorption, is a reduction of the steepness of the shock front. The effect of dissipation is larger for the linear waveform than for the nonlinear waveform. This is a consequence of nonlinear wave steepening, which counteracts the steepness reduction by the dissipation.

Figure 14 shows a spectral analysis of the effect of dissipation for $f_{\mathrm{ref}} = 2$ kHz. The waveforms shown in Fig. 13 were converted to decidecade spectra of the sound exposure level, denoted as $L(f_{\mathrm{c}})$, where f_{c} is the decidecade center frequency (see Ref. 7). The figure shows the spectral SEL difference between the results with and without absorption, denoted as ΔL, and represented by the blue and red lines. The figure also shows the expected attenuation $\alpha(f_{\mathrm{ref}})(f/f_{\mathrm{ref}})^2 r$, for propagation over $r = c_0 t$, which is equal to 1.98 km for $t = 1.32$ s. The linear waveform results agree well with the expected attenuation, while the nonlinear waveform results are considerably lower due to the effect of wave steepening. The figure also shows the attenuation $\alpha(f)r$ for the general absorption coefficient $\alpha(f)$ instead of the quadratic expansion $\alpha(f_{\mathrm{ref}})(f/f_{\mathrm{ref}})^2$ corresponding with the dissipation term in Eq. (8). At frequency $f_{\mathrm{ref}} = 2$ kHz, the two are equal, but at high frequency the quadratic expansion yields a larger attenuation. The spectral results for $f_{\mathrm{ref}} = 500$ Hz are similar, but shifted such that the linear results are equal to $\alpha(f)r$ at 500 Hz. This explains why the effect of dissipation in Fig. 13 is larger for $f_{\mathrm{ref}} = 500$ Hz than for $f_{\mathrm{ref}} = 2$ kHz.

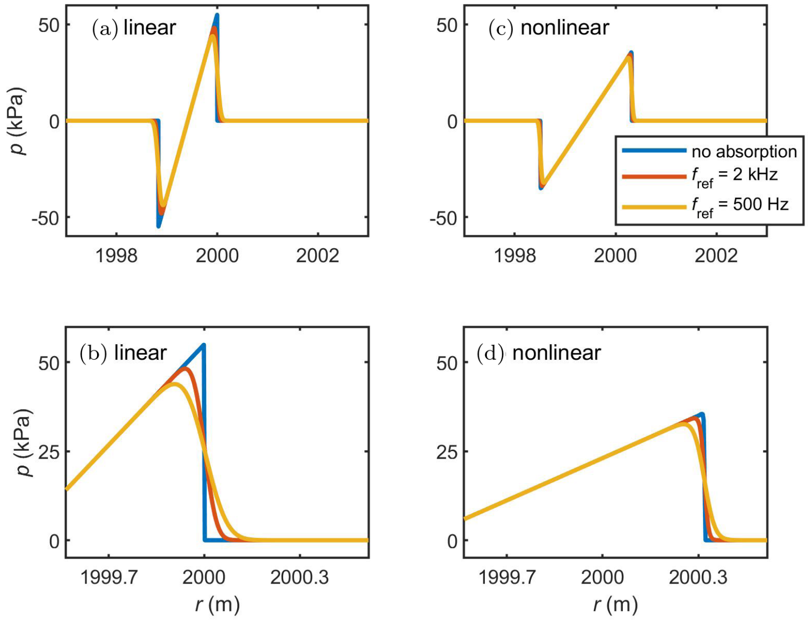

Fig. 13. Waveforms at time 1.32 s, calculated without absorption and with absorption, for $f_{\mathrm{ref}} = 500\,\mathrm{Hz}$ and 2 kHz. Graph (a) shows linear waveforms and graph (c) shows nonlinear waveforms. Graphs (b) and (d) zoom in on the leading shock.

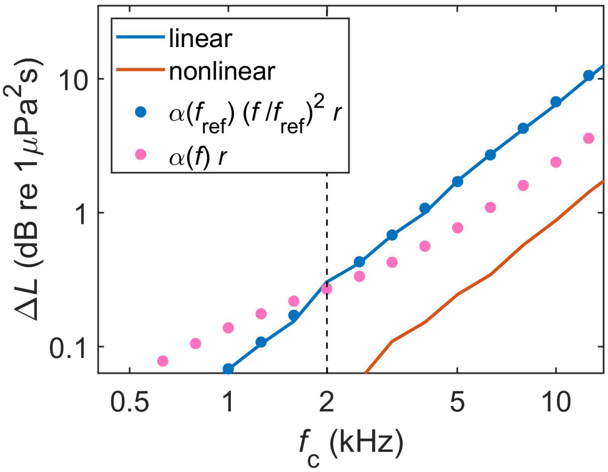

Fig. 14. Decidecade spectra of the effect of absorption on the SEL, for propagation over 1.98 km, with $f_{\mathrm{ref}} = 2\,\mathrm{kHz}$.

These results show that the effect of dissipation on the waveforms is small, for the cases considered in this article. We verified that this is also true for the case of nonlinear propagation in air, considered in Sec. 4.2. This conclusion agrees with a condition presented by Pierce[2] for the neglect of dissipation for weak-shock theory. The condition is that the following inequality must be satisfied:

$$\frac{\beta\, p\, \omega}{\rho_0\, c_0^3} > \alpha, \tag{62}$$

where p is a representative sound pressure. For the case considered above with $f_{\text{ref}} = 500\,\text{Hz}$, we have $\alpha = 3.23 \times 10^{-6}\,\text{Np/m}$. If we use $p = 50\,\text{kPa}$ and $f = 500\,\text{Hz}$, then the left-hand side of Eq. (62) becomes $1.7 \times 10^{-4}\,\text{m}^{-1}$, which is almost two orders of magnitude larger than the right-hand side.

4. Explosions in Water and in Air

The analytical and numerical methods described in Secs. 2 and 3 can be applied to spherical sound pulses generated by the detonation of explosives. In this section, we describe applications to underwater explosions and explosions in air. Analytical and numerical results are compared with experimental and numerical data from the literature.

4.1. *Underwater explosions*

Research on underwater explosions has a long history. In 1948, Cole[4] described experimental results and prediction models for underwater explosions. An underwater explosion generates a shock wave, followed by several weaker pulses, including cavitation-closure pulses related to reflections by the sea surface.[4,6,37–40]

Here, we focus on the shock wave, which can be approximated by an exponential waveform. Weston[6] notes that the approximation is good for the initial part of the waveform, while for large times the decay of the sound pressure is slower than exponential.

Parameters P and τ of the exponential waveform $p(t) = P \exp(-t/\tau)$ have been represented by the following empirical relations:[4–6,57]

$$P = 52.4 \times 10^6 \left(\frac{W^{1/3}}{r}\right)^{1.13}, \tag{63}$$

$$\tau = 92.5 \times 10^{-6} W^{1/3} \left(\frac{W^{1/3}}{r}\right)^{-0.22}, \tag{64}$$

where P is in units of Pascals, τ is in units of seconds, W is the explosive mass in kilograms TNT, and r is the distance from the source in meters. The relations were derived by regression on experimental data for different explosive masses:[5] 0.23, 11.3, 21.8, 24.9, and 34.5 kg TNT. The regressions were performed on P and $\tau/W^{1/3}$ as a function of scaled reciprocal distance $W^{1/3}/r$. The scaling of length and time with $W^{1/3}$ is based on the principle of similarity.[4] We refer to Eqs. (63) and (64) as Arons-Weston relations, in this article.

We have performed analytical and numerical calculations for a spherical exponential waveform (35) with $\phi_0 = 20\,\text{m}$. We assumed an explosive mass of 20 kg TNT and calculated parameters P and L from Eqs. (63) and (64) for $r = 20\,\text{m}$, using $L = c_0\tau$. The values of P and L are 5485.6 kPa and 0.5844 m, respectively, as in Secs. 3.2–3.6.

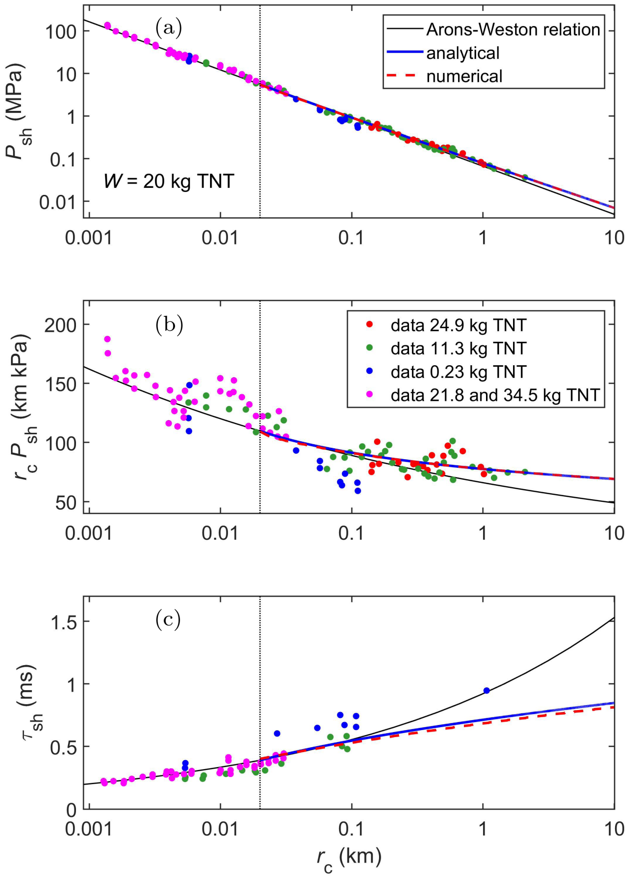

Fig. 15. Calculation and measurement results for shock pressure P_{sh} (a), product $r_{\mathrm{c}}P_{\mathrm{sh}}$ (b), and time constant τ_{sh} (c) as a function of range r_{c}, for an underwater explosion of 20 kg TNT. The vertical line at range 20 m indicates the starting range for the analytical and numerical solutions.

Figure 15 shows the calculation results, together with the experimental results from Arons,[5] scaled to 20 kg TNT, and the Arons-Weston relations for 20 kg TNT. The three graphs show shock pressure P_{sh}, product $r_{\mathrm{c}}P_{\mathrm{sh}}$, and time constant $\tau_{\mathrm{sh}} = L_{\mathrm{sh}}/c_0$ as a function of range r_{c}, up to a range of 10 km. We note that in the Arons-Weston relations (63) and (64), P_{sh} and τ_{sh} are denoted as P and τ. The experimental values of τ and the Arons-Weston relation (64) represent the initial decay of the peak pressure,[6] so we used calculated values for Fig. 15(c) that represent the slope of the waveform at the shock front, as described in Sec. 3.3. The analytical values of τ_{sh} were calculated with Eq. (43) from Sec. 3.3.

For ranges larger than about 0.1 km, the analytical and numerical results deviate considerably from the Arons-Weston relations. Graph (b) shows that the original data support the deviation for the shock pressure. Graph (c) shows that there is a single data point for 0.23 kg TNT at range 1 km that is responsible for the deviation for the time constant. As indicated by Rogers[16] and Best,[58] there is a considerable uncertainty in the experimental values of the time constant.

For comparison, we also applied the asymptotic formulation of the Kirkwood-Bethe theory[4,7] to calculate P_{sh} and τ_{sh} as a function of range. We found results close to the analytical and numerical results shown in Fig. 15. As indicated before, the Kirkwood-Bethe theory is based on the assumption that the waveform remains exponential, which is an approximation.[16]

The effect of the initial waveform on the analytical and numerical results in Fig. 15 can be inferred from Fig. 12. For example, with a Friedlander wave, we have a value of 64 km kPa for $r_{\mathrm{c}}P_{\mathrm{sh}}$ at range 1 km, while the value for the exponential wave is 78 km kPa. The experimental data around 1 km are closer to the value for the exponential wave than to the value for the Friedlander wave.

4.2. *Explosions in air*

Explosions in air generate sound pulses that can be modeled by a Friedlander function.[8–11] We focus on the positive phase of the waveform, with parameters P_{sh} and $\tau_{\mathrm{sh}} = L_{\mathrm{sh}}/c_0$. The negative phase of the Friedlander wave has no effect on these parameters.

Figure 16 shows results for an explosive of 20 kg TNT. For the analytical and numerical results shown in the figure, we used a Friedlander wave (49) with parameters $\phi_0 = 25\,\mathrm{m}$, $P = 10.84\,\mathrm{kPa}$ and $L = 3.305\,\mathrm{m}$. The values of P and L at 25 m were calculated from the

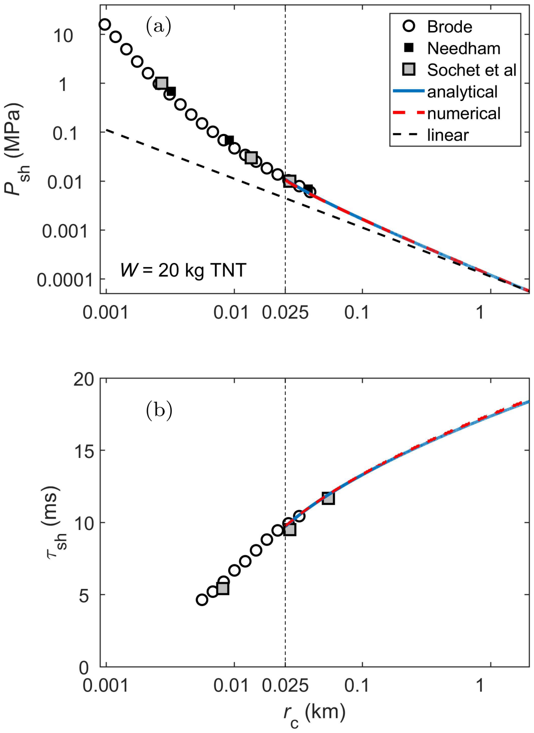

Fig. 16. Shock pressure P_{sh} (a) and time constant τ_{sh} (b) as a function of range r_{c}, for an explosion in air of 20 kg TNT. The vertical line at range 25 m indicates the starting range for the analytical and numerical solutions.

explosion energy, following the approach described in Ref. 11, which is based on the work of Pierce.[2] We assumed a value of 4.6 MJ/kg for the energy per unit mass of TNT, so the explosion energy, E, is equal to 92 MJ.

Pierce[2] used the positive phase of a spherical N wave as an approximation for the waveform generated by the sudden release of energy in a point. He used numerical fluid-dynamical results of Brode[18,19] to determine the values of P and $T(= L/c_0)$ of the N wave at a reference distance, and applied nonlinear propagation theory to obtain values at other distances. In Ref. 11, this approach has been used to derive an analytical expression for the sound exposure level spectrum of an explosion, assuming a Friedlander waveform.

The analytical and numerical results shown in Fig. 16 are in good agreement with each other. The results cover the range from $r_\mathrm{c} = 25\,\mathrm{m}$ to $r_\mathrm{c} = 2\,\mathrm{km}$. The shock pressure decreases with range and approaches the linear $1/r_\mathrm{c}$ behavior at large range. The time constant increases with range, from about 9.8 ms at 25 m to 18.4 ms at 2 km.

The analytical and numerical results are in line with the results of Brode,[18,19] Needham,[20] and Sochet *et al.*,[9] which are included in Fig. 16. These results were obtained from the graphs in the publications. The results were presented in the publications as scaled quantities, with distance and time expressed in units proportional to $E^{1/3}$. For Fig. 16, we converted the scaled results to results for an explosive mass of 20 kg TNT. The results of Needham and Sochet *et al.* are for a few selected ranges, while the results of Brode cover a broad interval of ranges.

The results of Brode[18,19] are based on numerical calculations for spherical blast waves, which were generated by the sudden release of energy in a point or in a small spherical region. The equations of fluid dynamics, representing conservation of mass, momentum, and energy, were integrated for an ideal gas and for air, including artificial viscosity to handle shocks. The results of Needham[20] represent experimental data for explosions. The results of Sochet *et al.*[9] represent numerical calculations of spherical blast waves, generated by an explosive with a mass of 1 kg TNT. These authors used various types of commercial software for simulating the generation and propagation of blast waves, based on integration of the equations of fluid dynamics.

It is of interest to consider how the calculation results in Fig. 16 depend on the assumption that the initial waveform is a Friedlander function. For the Friedlander function, we have a value of 56 Pa for P_sh at range 2 km. If we assume an exponential wave instead of a Friedlander wave, with equal values of P, L, and ϕ_0, then we find a value of 74 Pa. Similarly, the value of $\tau_\mathrm{sh} = L_\mathrm{sh}/c_0$ at range 2 km is 18.4 ms for the Friedlander wave, while the value of $\tau'_\mathrm{sh} = L'_\mathrm{sh}/c_0$ for the exponential wave is 20.1 ms. For the N wave, the values are 67 Pa and 19.7 ms, respectively. These values apply also to the triangular approximation of the waveform by a half N wave, which was mentioned in Sec. 1.

5. Conclusions

In this article, we have presented analytical and numerical calculations of the propagation of sound pulses with shocks. The results provide insight into the variation with range of the shock wave parameters P_{sh} and L_{sh}, and the waveform and the sound exposure integral over the waveform. The functions $P_{\text{sh}}(r)$ and $L_{\text{sh}}(r)$ have been compared with each other for three initial waveforms with shocks: an N wave, an exponential wave, and a Friedlander wave. Differences were explained by considering the shape of the waveform just behind the shock front. The expressions for the sound exposure integral show that the N wave remains an N wave during nonlinear propagation, while the exponential waveform does not remain exponential and the Friedlander waveform does not remain a Friedlander. For an initial sine waveform, we have shown that the asymptotic waveform for $t \to \infty$ is an N wave, which was confirmed by the asymptotic value of the sound exposure integral.

In Sec. 1, we mentioned the difference in nonlinear pulse broadening, as represented by the function $\tau_{\text{sh}}(r)$, between two analytical solutions presented in the literature: a solution for an exponential wave[16] and a solution for an N wave.[2] We have shown that the difference originates primarily from a difference in the definition of the time constant, while the effect of the difference in initial waveform is much smaller.

The analytical method used in this article is based on an explicit characteristics solution, with shocks derived from the equal-area rule. The equal-area rule can be evaluated analytically for simple waveforms. For more complex waveforms, a numerical element must be added to the analytical evaluation of the equal-area rule. This was illustrated for the Friedlander waveform.

The numerical finite-difference method presented in this article can be used for arbitrary waveforms. We found good agreement between analytical and numerical results, which demonstrates the accuracy of the numerical method. The numerical method was used to investigate the effect of dissipation of acoustic energy in the fluid, which counteracts the steepening of the shock front by nonlinear waveform distortion. The numerical method is computationally efficient, as it employs a frame that moves along with the sound pulse on a one-dimensional grid.

Experimental and numerical data from the literature for explosions in water and in air have been compared with analytical and numerical calculation results. The comparisons were performed for an explosive mass of 20 kg TNT, using similarity scaling for the conversion of the data.

For underwater explosions, the comparison includes experimental data for various explosive masses. The comparison also includes the widely-used Arons-Weston relations, which are based on regression analysis of the data. For ranges larger than about 0.1 km, the analytical and numerical results deviate from the Arons-Weston relations. For the shock pressure, P_{sh}, the deviation is small and is supported by the data. For the time constant, τ_{sh}, the deviation is larger and was attributed to uncertainty in the experimental data.

For explosions in air, the data from the literature are restricted to small ranges, and we found good agreement with the analytical and numerical results. For larger ranges, up to 2 km, the analytical and numerical results illustrate the effects of nonlinear waveform distortion.

ORCID

E.M. Salomons https://orcid.org/0000-0003-4919-6174

References

1. G.B. Whitham. *Linear and nonlinear waves.* Wiley, New York, 1974.
2. A.D. Pierce. *Acoustics. An introduction to its physical principles and applications*, chapter 11. AIP, New York, 1991.
3. D.T. Blackstock, M.F. Hamilton, and A.D. Pierce. Progressive waves in lossless and lossy fluids. In M.F. Hamilton and D.T. Blackstock, editors, *Nonlinear acoustics*, chapter 4. ASA Press Springer (open access, https://www.oapen.org/), 2024.
4. R.H. Cole. *Underwater Explosions, 1st ed.* Princeton University Press, Princeton, NJ, 1948.
5. A.B. Arons. Underwater explosion shock wave parameters at large distances from the charge. *J. Acoust. Soc. Am.*, **26**:343–346, 1954.
6. D.E. Weston. Underwater explosions as acoustic sources. *Proc. Phys. Soc.*, **76**:223–249, 1960.
7. E.M. Salomons, J.T. Tuitman, A.M. von Benda-Beckmann, and G.N. Peixoto Dourado. Numerical study of sound of underwater explosions in deep water and shallow water. *J. Acoust. Soc. Am.*, **158**:135–153, 2025.
8. F.G. Friedlander. The diffraction of sound pulses. I. Diffraction by a semi-infinite plane. *Proc. R. Soc. Lond. A*, **186**:322–344, 1946.
9. I. Sochet, D. Gardebas, S. Calderara, Y. Marchal, and B. Longuet. Blast wave parameters for spherical explosives detonation in free air. *Open Journal of Safety Science and Technology*, **1**:31–42, 2011.
10. I. Sochet (Ed.). *Blast effects. Physical properties of shock waves.* Springer, Cham, Switzerland, 2018.
11. E.M. Salomons. Analytical model for sound of explosives and firearms. *J. Acoust. Soc. Am.*, **156**:2034–2044, 2024.
12. L. Liu, R. Guo, K. Gao, and M.C. Zeng. Full-field peak pressure prediction of shock waves from underwater explosion of cylindrical charges. *Propellants Explos. Pyrotech.*, **42**:912–920, 2017.
13. P. Sherkar, J. Shin, A. Whittaker, and A. Aref. Influence of charge shape and point of detonation on blast-resistant design. *J. Struct. Eng.*, **142**:04015109, 2016.
14. C. Knock, N. Davies, and T. Reeves. Predicting blast waves from the axial direction of a cylindrical charge. *Propellants Explos. Pyrotech.*, **40**:169–179, 2015.
15. H. Qin, Y.L. Liu, Z.L. Tian, W.T. Liu, and S.P. Wang. Numerical investigation of the underwater explosion of a cylindrical explosive with the Eulerian finite-element method. *Phys. Fluids*, **36**:016104, 2024.
16. P.H. Rogers. Weak-shock solution for underwater explosion shock waves. *J. Acoust. Soc. Am.*, **62**:1412–1419, 1977.
17. M.F. Hamilton and C.L. Morfey. Model equations. In M.F. Hamilton and D.T. Blackstock, editors, *Nonlinear acoustics*, chapter 3. ASA Press Springer (open access, https://www.oapen.org/), 2024.
18. H.L. Brode. Numerical solutions of spherical blast waves. *J. Appl. Phys.*, **26**:766–775, 1955.
19. H.L. Brode. Blast wave from a spherical charge. *Phys. Fluids*, **2**:217–229, 1959.
20. C.E. Needham. *Blast waves.* Springer, Berlin, 2010.
21. P.H. Dahl, A.K. Jenkins, B. Casper, S.E. Kotecki, V. Bowman, C. Boerger, D.R. Dall'Osto, M.A. Babina, and A.N. Popper. Physical effects of sound exposure from underwater explosions on Pacific sardines (Sardinops sagax). *J. Acoust. Soc. Am.*, **147**:2383–2395, 2020.

22. B.L. Southall, J.J. Finneran, C. Reichmuth, P.E. Nachtigall, D.R. Ketten, A.E. Bowles, W.T. Ellison, D.P. Nowacek, and P.L. Tyack. Marine mammal noise exposure criteria: Updated scientific recommendations for residual hearing effects. *Aquat. Mamm.*, **45**:125–132, 2019.
23. S. P. Robinson, L. Wang, S. Cheong, P.A. Lepper, J.P. Hartley, P.M. Thompson, E. Edwards, and M. Bellman. Acoustic characterisation of unexploded ordnance disposal in the North Sea using high order detonations. *Mar. Pollut. Bull.*, **184**:114178, 2022.
24. A.M. von Benda-Beckmann, G. Aarts, H.Ö. Sertlek, K. Lucke, W.C. Verboom, R.A. Kastelein, D.R. Ketten, R. van Bemmelen, F.A. Lam, R.J. Kirkwood, and A.M. Ainslie. Assessing the impact of underwater clearance of unexploded ordnance on harbour porpoises (Phocoena phocoena) in the southern North Sea. *Aquat. Mamm.*, **41**:503–523, 2015.
25. P.D. Schomer. Assessment of community response to impulsive noise. *J. Acoust. Soc. Am.*, **77**:520–535, 1985.
26. J. Vos. A- and C-weighted sound levels as predictors of the annoyance caused by shooting sounds, for various façade attenuation types. *J. Acoust. Soc. Am.*, **113**:336–347, 2003.
27. M. Brink and J.M. Wunderli. A field study of the exposure-annoyance relationship of military shooting noise. *J. Acoust. Soc. Am.*, **127**:2301–2311, 2010.
28. E.M. Salomons, F.J.M. van der Eerden, and F.H.A. van den Berg. Model calculations and measurements of shooting sound in practical situations. *J. Acoust. Soc. Am.*, **155**:1162–1181, 2024.
29. G.B. Whitham. The flow pattern of a supersonic projectile. *Comm. Pure Appl. Math.*, **5**:301–348, 1952.
30. V.W. Sparrow. Lowering the boom. *Acoustics Today*, **2**:20–28, 2006.
31. J. Varnier and F. Sourgen. The ballistic wave, from rifle bullet to Apollo command module. *Acoustics in Practice*, **2**:43–51, 2014.
32. J. Varnier, M. Le Pape, and F. Sourgen. On the ballistic wave from projectiles and vehicles of simple geometry. *AIAA J.*, **56**:2725–2742, 2018.
33. A. Emmanuelli, D. Dragna, S. Ollivier, and P. Blanc-Benon. Sonic boom propagation over real topography. *J. Acoust. Soc. Am.*, **154**:16–27, 2023.
34. E.M. Salomons. A coherent line source in a turbulent atmosphere. *J. Acoust. Soc. Am.*, **105**:652–657, 1999.
35. B.E. McDonald and W. A. Kuperman. Time domain formulation for pulse propagation including nonlinear behavior at a caustic. *J. Acoust. Soc. Am.*, **81**:1406–1417, 1987.
36. Y. Yu, X. He, Y. Yang, R. Guo, and P. Song. Mach stem evolution and shock wave propagation mechanism in double-charge synchronous underwater explosions. *Phys. Fluids*, **37**:084111, 2025.
37. F.A. Costanzo and J.D. Gordon. A solution to the axisymmetric bulk cavitation problem. https://apps.dtic.mil/sti/tr/pdf/ADA134453.pdf, 1983. 53rd Shock and Vibration Bulletin, Shock and Vibration Information Center, Naval Research Laboratory, Washington, D.C.
38. F.A. Costanzo. Underwater explosion phenomena and shock physics. https://www.researchgate.net/publication/251393757_Underwater_Explosion_Phenomena_and_Shock_Physics, 2011.
39. N.R. Chapman. Measurement of the waveform parameters of shallow explosive charges. *J. Acoust. Soc. Am.*, **78**:672–681, 1985.
40. D.R. Dall'Osto, P. Dahl, and N.R. Chapman. The sound from underwater explosions. *Acoustics Today*, **19**:12–19, 2023.
41. E.M. Salomons. *Computational atmospheric acoustics*. Kluwer, Dordrecht, 2001.
42. A. Emmanuelli, D. Dragna, S. Ollivier, and P. Blanc-Benon. Characterization of topographic effects on sonic boom reflection by resolution of the Euler equations. *J. Acoust. Soc. Am.*, **149**:2437–2450, 2021.

43. C.L. Morfey and F.D. Cotaras. Propagation in inhomogeneous media (ray theory). In M.F. Hamilton and D.T. Blackstock, editors, *Nonlinear acoustics*, chapter 12. ASA Press Springer (open access, https://www.oapen.org/), 2024.
44. R.T. Beyer. The parameter B/A. In M.F. Hamilton and D.T. Blackstock, editors, *Nonlinear acoustics*, chapter 2. ASA Press Springer (open access, https://www.oapen.org/), 2024.
45. D.T. Blackstock. On plane, spherical, and cylindrical sound waves of finite amplitude in lossless fluids. *J. Acoust. Soc. Am.*, **36**:217–219, 1964.
46. D.T. Blackstock. Nonlinear acoustics (theoretical). In D.E. Gray, editor, *American Institute of Physics Handbook*, chapter 3n. McGraw-Hill, New York, 1972.
47. J.H. Ginsberg and M.F. Hamilton. Computational methods. In M.F. Hamilton and D.T. Blackstock, editors, *Nonlinear acoustics*, chapter 11 (Section 11.3.2). ASA Press Springer (open acces, https://www.oapen.org/s), 2024.
48. B.E. McDonald and J. Ambrosiano. High-order upwind flux methods for scalar hyperbolic conservation laws. *J. Comp. Phys.*, **56**:448–460, 1984.
49. J.P. Boris and D.L. Book. Flux-corrested transport. I. SHASTA, a fluid transport algorithm that works. *J. Comp. Phys.*, **11**:38–69, 1973.
50. W. Lauterborn, T. Kurz, and I. Akhatov. Nonlinear acoustics in fluids. In T.D. Rossing, editor, *Springer Handbook of Acoustics*, chapter 8. Springer, 2014.
51. D.T. Blackstock. Connection between the Fay and Fubini solutions for plane sound waves of finite amplitude. *J. Acoust. Soc. Am.*, **39**:1019–1026, 1966.
52. F. Coulouvrat. A quasi-analytical shock solution for general nonlinear progressive waves. *Wave Motion*, **46**:97–107, 2009.
53. B. Persson. Comment on "Weak-shock solution for underwater explosion shock waves". *J. Acoust. Soc. Am.*, **66**:308, 1979.
54. F. Jensen, W. Kuperman, M. Porter, and H. Schmidt. *Computational Ocean Acoustics*. Springer, Heidelberg, 2011.
55. ISO 9613-1:1993. Acoustics — Attenuation of sound during propagation outdoors – Part 1: Calculation of the absorption of sound by the atmosphere, 1993. International Organization for Standardization, Geneva, Switzerland.
56. P.V. Yuldashev, M.V. Averiyanov, V.A. Khokhlova, S. Ollivier, and P. Blanc-Benon. Nonlinear spherically divergent shock waves propagating in a relaxing medium. *Acoust. Phys.*, **54**:32–41, 2008.
57. M.A. Ainslie. *Principles of sonar performance modelling*. Springer, Berlin, 2010.
58. J.P. Best. *The dynamics of underwater explosions*. PhD thesis, University of Wollongong, 1991. https://ro.uow.edu.au/.